iScience

CellPress

Article

Mesoporous TiO_2/TiC@C Composite Membranes with Stable TiO_2-C Interface for Robust Lithium Storage

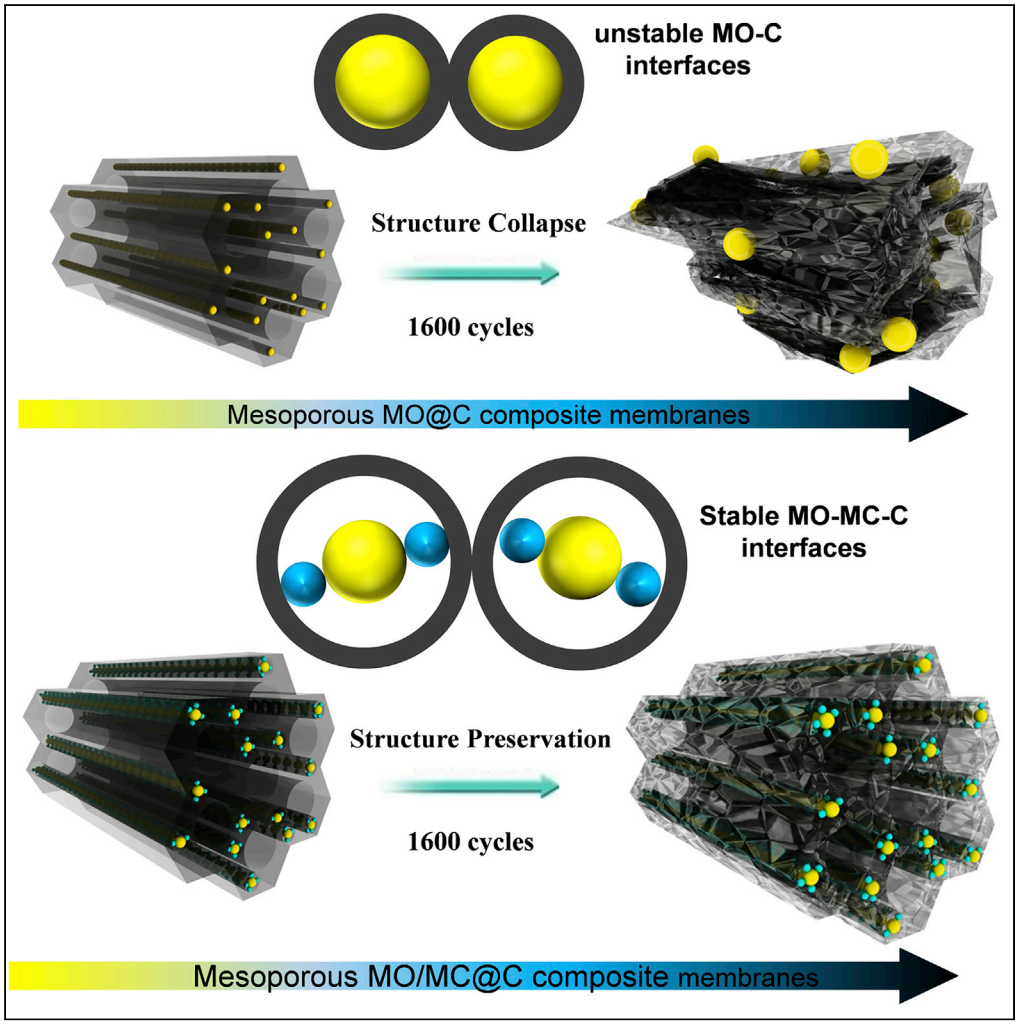

Wei Zhang, Lianhai Zu, Biao Kong, ..., Yang Liu, Jinhu Yang, Dongyuan Zhao

yangjinhu@tongji.edu.cn (J.Y.)
dyzhao@fudan.edu.cn (D.Z.)

HIGHLIGHTS

Mesoporous TiO_2/TiC@C membranes were synthesized by a simple method

This method can be extended to the synthesis of other metal oxide/metal carbide@C

The TiC nanodots can alleviate tensile and compression stress effect upon lithiation

Long working life and excellent rate performance can be achieved

Zhang et al., iScience 3, 149–160
May 25, 2018
https://doi.org/10.1016/j.isci.2018.04.009

iScience

CellPress

Article

Mesoporous TiO_2/TiC@C Composite Membranes with Stable TiO_2-C Interface for Robust Lithium Storage

Wei Zhang,[1,4] Lianhai Zu,[2,3,4] Biao Kong,[1] Bingjie Chen,[2] Haili He,[1] Kun Lan,[1] Yang Liu,[1] Jinhu Yang,[2,3,*] and Dongyuan Zhao[1,5,*]

SUMMARY

Transition metal oxides/carbon (TMOs/C) composites are important for high-performance lithium-ion batteries (LIBs), but the development of interface-stable TMOs/C composite anodes for robust lithium storage is still a challenge. Herein, mesoporous TiO_2/TiC@C composite membranes were synthesized by an *in situ* carbothermic reduction method. TiC nanodots with high conductivity and electrochemical inactivity at the TiO_2-C interface can significantly enhance the electrical conductivity and structural stability of the membranes. Finite element simulations demonstrate that the TiO_2/TiC@C membranes can effectively alleviate tensile and compression stress effects upon lithiation, which is beneficial for robust lithium storage. When used as additives and binder-free electrodes, the TiO_2/TiC@C membranes show excellent cycling capability and rate performance. Moreover, a flexible full battery can be assembled by employing the TiO_2/TiC@C membranes and shows good performance, highlighting the potential of these membranes in flexible electronics. This work opens an avenue to constructing interface-stable composite structures for the next-generation high-performance LIBs.

INTRODUCTION

Lithium-ion batteries (LIBs) are widely used in portable electric devices and electric vehicles (Armand and Tarascon, 2008; Aricò et al., 2005; Larcher and Tarascon, 2015). Extensive research has been carried out to develop transition metal oxides (TMOs)-based composite materials as LIB anodes (Yu et al., 2017a; Jeong et al., 2013; Su et al., 2013; Yu et al., 2017b; Peng et al., 2012; Wang et al., 2016a; Wang et al., 2013; Wang et al., 2015; Gu et al., 2015; Cai et al., 2014; Guan et al., 2016; Armstrong et al., 2006). In most cases, carbon materials including mesoporous carbon, carbon nanotubes, and graphene are employed as ideal matrixes for TMOs anodes owing to their unique properties such as excellent conductivity and flexibility, which can facilitate stable and fast lithium storage (Zhang et al., 2014; Fang et al., 2016; Mo et al., 2017). However, current TMOs/C composite anodes still suffer from poor cycling stability due to unstable TMOs-C interfaces resulting from the volume change difference between carbon and TMOs upon Li^+ insertion/extraction. The unstable TMOs-C interfaces may cause aggregation of TMOs nanoparticles as well as collapse of carbon frameworks. As a result, the cycling life over 1,000 cycles based on TMOs/carbon composites have been extremely limited. Therefore the construction of stable TMOs-carbon interfaces is the key for stable and robust lithium storage, which remains a considerable challenge.

Among the different kinds of TMOs, TiO_2 is an attractive material for LIBs owing to its natural abundance, low cost, and environmental benignancy (Liu and Chen, 2014; Liu et al., 2015a; Zhang et al., 2012). TiO_2/C composite anode materials with various dimensions and structures have been fabricated, which include hierarchical TiO_2/C nanocomposite monoliths (Huang et al., 2016), ordered mesoporous TiO_2/C nanocomposites (Zeng et al., 2013), graphitic carbon conformal coating of mesoporous TiO_2 hollow spheres (Liu et al., 2015b), and mesoporous TiO_2 coating on flexible graphitized carbon (Liu et al., 2016). However, all TiO_2/C composites also suffer from severe structural collapse stemming from unstable TiO_2-C interfaces. In this regard, TiO_2/C composite represents a typical class of LIB anode materials facing the problem of serious structure disintegration. Therefore there is a pressing need to solve the aforementioned problem of TiO_2/C composite.

Herein, to construct stable TiO_2-C interfaces, TiC nanodots with high conductivity and electrochemical inactivity (Wang et al., 2016b; Yao et al., 2011; Peng et al., 2016; Allcorn and Manthiram, 2015) are

[1]Department of Chemistry, State Key Laboratory of Molecular Engineering of Polymers, Shanghai Key Lab of Molecular Catalysis and Innovative Materials, Laboratory of Advanced Materials and iChEM, Fudan University, Shanghai 200433, P. R. China

[2]School of Chemical and Engineering, Tongji University, Siping Road 1239, Shanghai 200092, P. R. China

[3]Research Center for Translational Medicine & Key Laboratory of Arrhythmias of the Ministry of Education of China, East Hospital, Tongji University School of Medicine, No. 150 Jimo Road, Shanghai 200120, P. R. China

[4]These authors contributed equally

[5]Lead Contact

*Correspondence: yangjinhu@tongji.edu.cn (J.Y.), dyzhao@fudan.edu.cn (D.Z.)

https://doi.org/10.1016/j.isci.2018.04.009

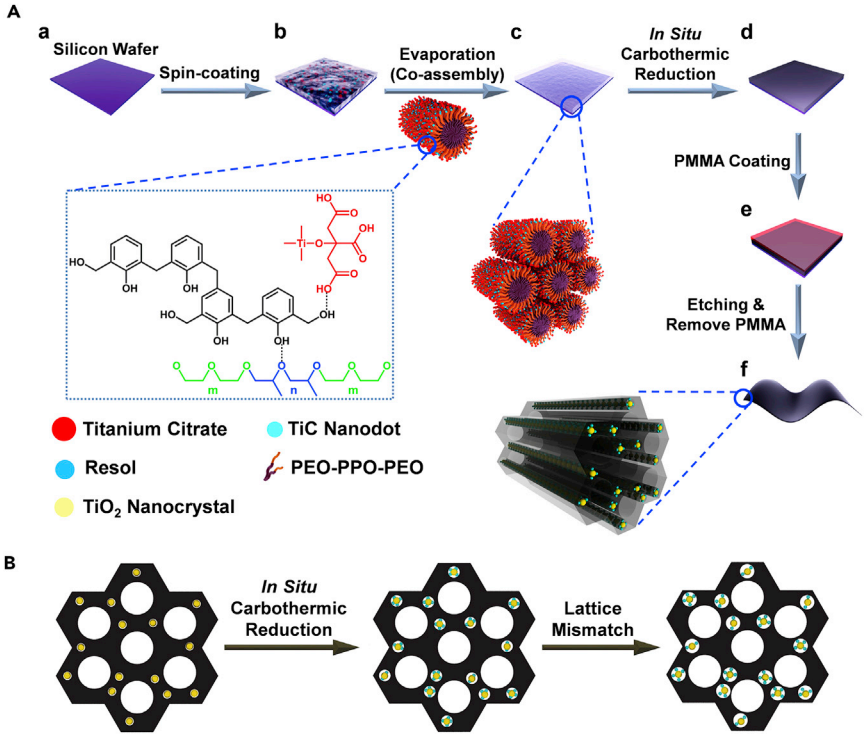

Figure 1. Design and Material Synthesis

(A) Schematic illustration of the synthesis of mesoporous TiO_2/TiC@C composite membranes via a facile *in situ* carbothermic reduction strategy.

(B) Schematic illustration of structure evolution during the *in situ* carbothermic reduction.

introduced to TiO_2-C interfaces by an *in situ* carbothermic reduction (Yu et al., 2007) that occurs in TiO_2-nanocrystals-embedded mesoporous carbon framework (TiO_2@C) membranes. The designed strategy leads to the formation of stable TiO_2-C interfaces where TiC nanodots act as a bridge to link TiO_2 nanocrystals and carbon frameworks accurately. The obtained mesoporous TiO_2/TiC@C composite membranes have a conductive, robust, and mesoporous framework. Besides, TiO_2 nanocrystals and TiC nanodots are interconnected and highly dispersed in the mesoporous carbon frameworks. When used as additive-free and binder-free electrodes, the TiO_2/TiC@C membranes deliver a high capacity of ~237 $mA{\cdot}h{\cdot}g^{-1}$ at a current density of 0.4 $A{\cdot}g^{-1}$. More importantly, an ultra-long cycling life (up to 5,000 cycles with over 68.4% reversible capacity retention) and superior rate performance can be achieved. Furthermore, a flexible full battery with impressive battery performance was assembled by using the TiO_2/TiC@C membranes as the anode, highlighting the great potential of the composite membranes in flexible devices.

RESULTS

Design and Material Synthesis

The mesoporous TiO_2/TiC@C composite membranes can be synthesized through a simple co-assembly/*in situ* carbothermic reduction route (see Transparent Methods) by using resol, titanium citrate complex, and pluronic F127 as the carbon precursor, titanium precursor, and template, respectively. First, a pretreated silicon wafer (Figure 1A, panel a) with thin oxidation layers on the surface was selected as a substrate, and the homogeneous solution containing resol, titanium citrate complex, and F127 was coated on the substrate by a spin-coating method (Figure 1A, panel b). A dry thin membrane was obtained after evaporation of solvents (Figure 1A, panel c), and mesoporous TiO_2/TiC@C composite membranes (Figure 1A, panel d) were obtained after further carbothermic reduction in nitrogen atmosphere at 900°C (Huang et al., 2010). In this process, titanium citrate clusters was transformed into TiO_2 nanocrystals and mesoporous TiO_2@C composite membranes were formed first. With the temperature increasing, an *in situ* carbothermic reduction occurred at the TiO_2-C interface and then TiC nanodots were formed

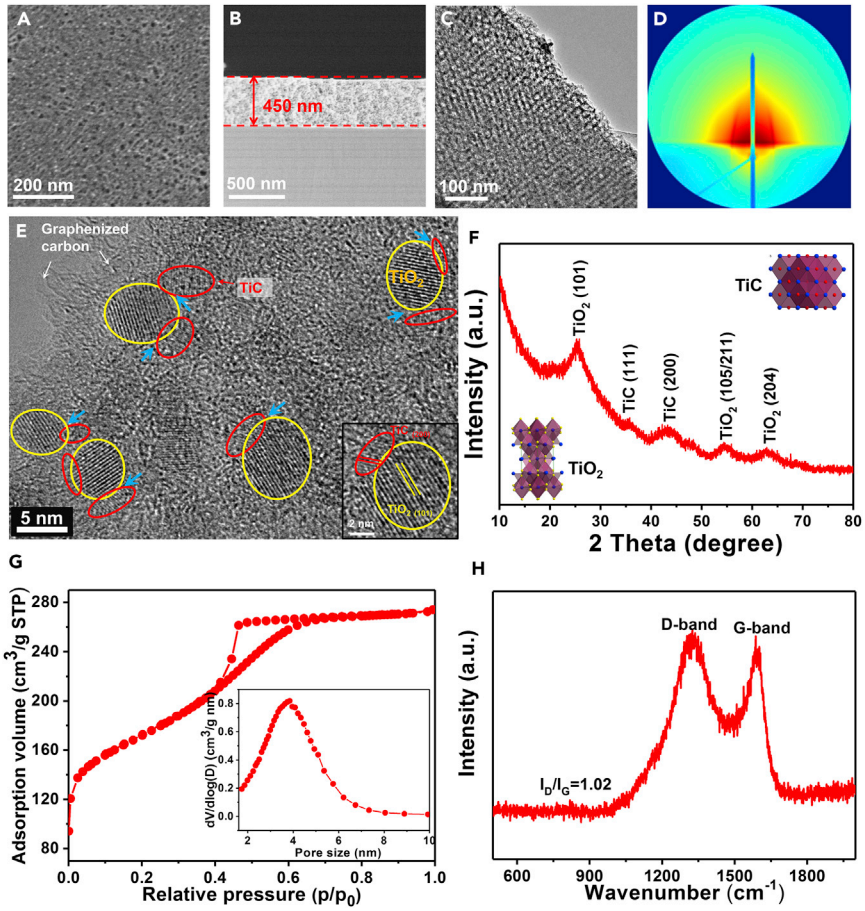

Figure 2. Structure and Composition Characterizations of the Mesoporous TiO_2/TiC@C Composite Membranes

(A) Top-view scanning electron microscopic image.

(B) Cross-sectional scanning electron microscopic image.

(C) Low-magnification TEM image.

(D) GISAXS image.

(E)High-resolution TEM image. The blue arrows indicate the TiO_2-TiC interfaces.

(F) XRD pattern, the insets in (F) show the molecular structures of TiO_2 and TiC crystals.

(G) N_2 adsorption-desorption isotherms and the corresponding pore size distribution (inset).

(H) Raman spectrum.

See also Figures S1–S10.

between the TiO_2 nanocrystals and carbon frameworks (Figure 1B). To obtain free-standing membranes, a polymethyl methacrylate (PMMA) thin film was introduced onto the surface of TiO_2/TiC@C membranes (Figure 1A, panel e). After the silica layer was etched by using a KOH solution (10 wt %) and the PMMA thin film was removed by anisole solvent (Feng et al., 2011), a free-standing membrane was obtained (Figure 1A, panel f). To deeply understand the role of the unique structure of the TiO_2/TiC@C membranes in lithium storage, mesoporous TiO_2@C composite membranes were selected and examined for comparison.

Structural and Composition Characterizations

The top-view field emission scanning electron microscopic (FESEM) images (Figures 2A and S1A) show that the TiO_2@C and TiO_2/TiC@C membranes have a smooth and continuous surface with stripe-like, hexagonally arranged mesopores. A uniform thickness of ~450 nm of the TiO_2/TiC@C membrane is observed by a cross-sectional FESEM image (Figure 2B), showing a small shrinkage of 10% compared with ~500 nm of the pristine TiO_2@C membranes (Figure S1B). It should be noted here that the thickness of the membranes can

be easily controlled by changing the rotation speed. Transmission electron microscopic (TEM) images (Figures 2C and S1C) of the TiO_2@C and TiO_2/TiC@C membranes show a well-defined 2D porous structure consisting of ordered hexagonal-patterned mesopores with an average diameter of ~4 nm, which is consistent with the observation in the top-view FESEM images (Figures 2A and S1A). Further evidences for the ordered mesoporous structure can be obtained from glancing incidence small-angle X-ray diffraction (GISAXS, Figures 2D and S1D) and small-angle X-ray diffraction (SAXS, Figure S2) patterns.

A high-resolution transmission electron microscopic (HRTEM) image of the TiO_2/TiC@C membranes (Figure 2E) shows that TiC nanodots (~2 nm) are formed at the TiO_2-C interface as a bridge between TiO_2 nanocrystals and carbon frameworks. Compared with pristine TiO_2 nanocrystals (~7 nm) in the TiO_2@C membranes (Figure S1E), the size of TiO_2 nanocrystals decreases because the formation of TiC nanodots is at the expense of TiO_2 nanodots in the *in situ* carbothermic reduction. The crystal lattices are clearly observed (inset Figure 2E), with distances of 0.21 and 0.35 nm corresponding to the (200) plane of cubic structured TiC (JCPDS No. 32-1383) and the (101) plane of tetragonal structured anatase TiO_2 (JCPDS No. 21-1272), respectively. The phase transformation (from TiO_2 to TiC) is further confirmed by X-ray diffraction (XRD), X-ray photoelectron spectroscopy (XPS), and X-ray absorption fine structure spectroscopy (XANFS). The XRD pattern of the mesoporous TiO_2/TiC@C composite membranes (Figure 2F) exhibits broad diffraction peaks indexed to TiO_2 and TiC phases, in accordance with the results of HRTEM. No rutile can be detected, because amorphous carbon can act as an inhibitor for grain growth of TiO_2 nanocrystals and causes the suppression of phase transition from anatase to rutile nanocrystals (Huang et al., 2010). The XPS spectra (Figure S3) of the TiO_2@C and TiO_2/TiC@C membranes reveal three main peaks at approximately 284, 458, and 530 eV, which are associated with the spin states of C_{1s}, Ti_{2p}, and O_{1s}, respectively. From high-resolution XPS spectra (Figures S4 and S5), a shift of Ti_{2p} and C_{1s} can be observed between TiO_2@C and TiO_2/TiC@C composite, which may be attributed to the formation of the TiC nanodots. The Ti_{2p} peak at a low bonding energy (Figure S6) is assigned to O-Ti-C bond (Shan et al., 2015; Kiran and Sampath, 2012), implying that TiO_2 nanocrystals and TiC nanodots are interconnected through chemical bonds. The Ti K-edge pre-edge XANFS (Figure S7) shows that the A1 and A2 per-peaks of the TiO_2/TiC@C membrane have a little shift compared with the TiO_2@C membranes, indicating the difference of coordination environment (Angelomé et al., 2007). The uniform distribution of C, Ti, and O can be observed by elemental mapping (Figures S8 and S9). These results clearly demonstrate that TiC nanodots are produced at the TiO_2-C interface through an *in situ* carbothermic reduction process.

The nitrogen sorption isotherms of the TiO_2@C and TiO_2/TiC@C composite membranes (Figures 2G and S1G) show representative type IV curves with H2 hysteresis loops, similar to those of the typical ordered mesoporous materials, revealing uniform pore size distribution. The pore size distribution derived from the adsorption branch using the Barrett-Joyner-Halenda (BJH) model shows uniform mesopores centered at 4.0 and 3.8 nm for the TiO_2@C and TiO_2/TiC@C membranes, respectively (insets in Figures 2G and S1G). The Brunauer-Emmett-Teller (BET) surface area of the TiO_2/TiC@C membranes is calculated to be 674 $m^2 \cdot g^{-1}$, which is slightly larger than that for the pristine TiO_2@C membranes (501 $m^2 \cdot g^{-1}$, Table S1), implying that more micropores are generated during the *in situ* carbothermic reduction process. In addition, the mass ratios of C, TiO_2, and TiC for the mesoporous TiO_2/TiC@C composite membranes are calculated to be 60:28:12 on the basis of thermogravimetric analysis (TGA) (Figure S10) before and after removal of the TiO_2 nanocrystals by using concentrated H_2SO_4. Raman spectra of the TiO_2@C and TiO_2/TiC@C membranes (Figures 2H and S1H) show sharp D and G peaks with a D/G intensity ratio of ~1:1, indicating the partial graphitization of the carbon matrixes (Kong et al., 2016).

Processing Feasibility and Scalability

It is worth mentioning that the membranes have a set of interesting properties, such as transferability, flexibility, tailorability, and large-scale production. Membranes supported by silicon wafer with an area of 1.5 cm × 1.5 cm can be peeled off to form an intact membrane with good flexibility (Figures S11A and S11B). These membranes can be transferred onto other substrates with the protection of PMMA, such as glass slides and glass rods, and can be bent without cracking (Figures S11C–S11F). Furthermore, the membranes supported by soft substrates can be conveniently tailored into desired shapes, such as square, circle, or triangle (Figures S11G–S11I). The high processing feasibility highlights the potential applications in a variety of important fields (e.g., sensor, battery, and adsorption).

More importantly, the synthesis for the mesoporous composite membranes can be scaled up. For instance, by using a large Ti foil (12 cm × 12 cm) as a substrate, a membrane with an area of ~144 cm^2 was produced (Figure S12). Moreover, the synthetic method can be extended to a large variety of substrates with different dimensions from one to three dimensions, such as W wires, Ti foils, and Cu foams (Figure S13). Therefore the synthetic strategy is highly versatile, which could be used for the synthesis of other mesoporous membranes.

Extension of the Synthetic Strategy to Other TMO/Carbon System

Significantly, this *in situ* carbothermic method is general and can be extended to the synthesis of other TMO/metal carbide@C systems. For example, the mesoporous $MoO_{2.80}/Mo_2C$@C composites can be synthesized by using molybdenyl acetylacetonate, phenolic resol, and pluronic F127 as molybdenum, carbon precursors, and template, respectively. The SAXS results show that the resultant $Mo_2C/MoO_{2.80}$@C composites possess ordered mesoporous structure (space group *p6mm*, Figure S14A). The XRD pattern (Figure S14B) of the mesoporous $Mo_2C/MoO_{2.80}$@C composites exhibits well-defined diffraction peaks, which can be indexed to Mo_2C (JCPDS No.15-0457) and $MoO_{2.80}$ (JCPDS No.12-0517), indicating the success of carbothermic reduction. The ordered mesoporous structure can be further confirmed by the TEM image (Figure S14C). Moreover, small nanoparticles with a uniform size of ~3 nm are embedded in the mesoporous carbon frameworks. The HRTEM image shows that Mo_2C nanodots are formed at the $MoO_{2.80}$-C interface (Figure S14D); the interplanar distances of ~0.24 and 0.29 nm are well matched with the *d*-spacing of the (111) plane of Mo_2C and the (1620) plane of $MoO_{2.80}$, respectively. These results demonstrate that the mesoporous $Mo_2C/MoO_{2.80}$@C composite has been successfully prepared by the *in situ* carbothermic reduction method and that the proposed synthetic strategy may be generally applicable to other TMO/carbon systems.

Electrochemical Performances

The synthesized mesoporous composite TiO_2@C and TiO_2/TiC@C membranes with thickness of ~5 μm (inset in Figure 3A) standing on Cu foil were directly used as anodes of LIBs without any conducting additives and binders. The electrochemical behaviors of the representative TiO_2/TiC@C and TiO_2@C membrane electrodes were characterized by cyclic voltammetry (CV) at a scanning rate of 0.5 $mV \cdot s^{-1}$ between 0.01 and 3.0 V (Figures 3A and S15). The first cathodic scan of the mesoporous TiO_2/TiC@C composites shows four peaks. The peak at 1.70 V can be assigned to Li^+ insertion into the lattices of anatase. Besides, the peaks at 1.31 and 0.62 V resulted from the formation of solid-electrolyte interface (SEI) on TiO_2 nanocrystals and carbon frameworks, respectively (Fang et al., 2013), while the peak at 1.0 V is attributed to the combined effect of the formation of SEI on TiO_2 and carbon (Zeng et al., 2013; Wang et al., 2016b). After the first cycle, two peaks, i.e., one anodic peak at 1.70 V and one cathodic peak at 2.05 V, are observed in the CV curves (Figure 3A), which are associated with the Li^+ insertion/extraction into/from the lattices of anatase TiO_2. It is found that the peak current in the first scan is much higher than the following ones owing to the formation of SEI layer on the surface of the electrode (Kaskhedikar and Maier, 2009). From the second cycle onward, the CV scans overlap substantially, indicating the outstanding reversibility of lithiation/delithiation over the TiO_2/TiC@C membrane electrode.

Rate performance of the mesoporous composite TiO_2/TiC@C electrodes was conducted at drastically varying current densities from 0.33 $A \cdot g^{-1}$ to as high as 10 $A \cdot g^{-1}$. At an extremely high current density of 10 $A \cdot g^{-1}$, a high capacity of 57 $mA \cdot h \cdot g^{-1}$ can be still retained, demonstrating the excellent rate performance (Figure 3B). The mesoporous TiO_2/TiC@C membrane electrode also demonstrates superior long cycling stability and high reversibility. The composite membrane electrode was examined up to 1,600 cycles at a discharge/charge current of 0.4 $A \cdot g^{-1}$ (Figure 3C). It can be seen that the TiO_2/TiC@C membrane electrode is able to maintain a specific reversible capacity of 244 $mA \cdot h \cdot g^{-1}$ after 1,600 cycles, with only 0.009% fading per cycle, which is ~23.7% of that (0.038% fading per cycle) for the pristine TiO_2@C membrane electrode at the same current density (Figure S16, Table S2). In addition, when an extremely long cycling test of 5,000 cycles is applied at a very high current density of 1.5 $A \cdot g^{-1}$, the TiO_2/TiC@C membrane electrode can still exhibit outstanding cycling stability. After a slow capacity fading in the initial dozens of cycles, a reversible capacity of 150 $mA \cdot h \cdot g^{-1}$ remains unchanged during the subsequent cycles, with coulombic efficiencies of nearly 100% (Figure 3C). Here, to clarify the effect of carbon on the performance of the TiO_2/TiC@C composites, mesoporous carbon annealed at 900°C with a high surface area (806 $m^2 g^{-1}$) and uniform pore size (4.0 nm) was synthesized and its electrochemical properties were measured (Figure S17). Compared with the TiO_2/TiC@C composites, the mesoporous carbon shows a much lower

capacity (~70 mA•h•g^{-1} at a current of 1.5 A g^{-1}, Figure S18) and initial coulomb efficiency (~12.8%), which are only ~46.7% and ~48.4% of those of the TiO_2/TiC@C electrode, respectively. Besides, the mesoporous carbon shows poor rate performance and the capacity delivered at specific current densities is ~21%–61% of that of the TiO_2/TiC@C composite electrode (Figure S18, Table S3). Furthermore, to clarity the effect of mass loading on the electrochemical performance, the mesoporous TiO_2/TiC@C membrane electrode as thick as ~30 μm was fabricated (Figure S19) and evaluated with related battery performance. It is found that the thicker TiO_2/TiC@C membrane electrode exhibits high capacity and excellent cycling stability (Figure S20), comparable to that of the typical thin membrane electrode.

Nyquist plots for the TiO_2/TiC@C membrane electrode (Figures 3D and 3E) exhibit a lower charge transfer resistance (Rct, 92 Ω) than those of the TiO_2@C membrane electrode (175 Ω), which can lead to faster lithium-ion diffusion. The sheet resistances of the TiO_2@C and TiO_2/TiC@C membranes (Figure S21) are measured to be 22.62 and 1.37 kΩ•sq^{-1}, respectively. To verify the effect of the mesoporous carbon component in the composites, the sheet resistance of the pristine mesoporous carbon (Figure S22) annealed at 700°C and 900°C was measured, and it was found to be 8.62 and 0.47 kΩ•sq^{-1}, respectively. Therefore the enhanced electric conductivity of the composite membrane can be assigned to the enhanced graphitization of carbon at a higher annealing temperature and the existence of the TiC nanodots owing to the significantly higher conductivity of TiC (~10^4 S•cm^{-1}) than TiO_2 (~10^{-10} S•cm^{-1}).

Assembly of a Flexible Full Cell

To solve the large Li consumption problem caused by SEI formation, the mesoporous TiO_2/TiC@C membranes were pre-lithiated before being used as an anode material for the assembly of full battery (Figure S23). The optical images (Figures 3F, 3G, S24, and S25A, Video S1) illustrate that the flexible full battery can successfully be assembled and is able to power a light-emitting diode (LED) under both flat and bent states with different bent angles (0, 30, 60, 90, 120, and 150°). The charge/discharge curves of the battery cycled at a current density of ~20 mA g^{-1} in the voltage window of 2.8–4.2 V is shown in Figure S24B. The battery exhibits good performance, and acceptable specific capacities of 116, 108, 103, 78, 62, and 53 mAh g^{-1} can be achieved with different bent angles of 0, 30, 60, 90, 120, and 150°, respectively. The results demonstrate the potential of the membranes in practical flexible electronics applications.

Electrochemical Kinetics Analysis

Kinetics analysis based on CV was carried out to gain further insight into the electrochemistry of the mesoporous TiO_2/TiC@C membrane electrode. The CV curves of the TiO_2/TiC@C membrane electrode at various scan rates from 2 to 200 mV•s^{-1} display similar shapes with broad peaks during both cathodic and anodic scans (Figure 4A). According to the relationship between the measured current (i) and the scan rate (v): $i = av^b$, where a and b are adjustable values (Augustyn et al., 2013), b can be determined by the slope of the log(v)–log(i) plots. A b value of 0.718 can be obtained, indicating that both the capacitive and diffusion-controlled processes contribute to the total capacity of the TiO_2/TiC@C membrane electrodes (Figure 4B). Quantitatively, 54.7% of the total charge (or capacity) is capacitive at a scan rate of 10 mV•s^{-1} (Figure 4C). Contribution ratios between the two different processes at other scan rates can also be quantified. The results show that the capacitance is improved gradually with increasing scan rate (Figure 4D). For the mesoporous carbon annealed at 900°C, the b value is calculated to be 0.705 (Figures S26 and S27), which is similar to that of the TiO_2/TiC@C composite. However, the capacitive contribution of the mesoporous carbon (35.3%) at 10 mV•s^{-1} is lower than that of the TiO_2/TiC@C composite. The higher capacitive contribution in the composite is probably caused by extra capacitive contribution of the TiO_2 nanocrystals (Kim et al., 2010). The prominent pseudocapacitive behavior in the TiO_2/TiC@C electrode is beneficial for fast charge storage and long-term cyclability.

Structural Evolution of Electrodes

The TEM image of the mesoporous TiO_2@C membrane electrode after 1,600 cycles at a current density of 0.4 A•g^{-1} (Figure 5A) shows that the size of TiO_2 nanocrystals largely increases and the mesostructure is completely collapsed. This result clearly indicates that TiO_2 nanocrystals got aggregated during Li^+ insertion/extraction processes, which in turn results in the collapse of the mesoporous structure of the carbon matrix. Unfortunately, a thick SEI film is formed on the surface of the TiO_2 nanocrystals, which would decrease the conductivity of the electrode. A similar structure damage is also observed in mesoporous

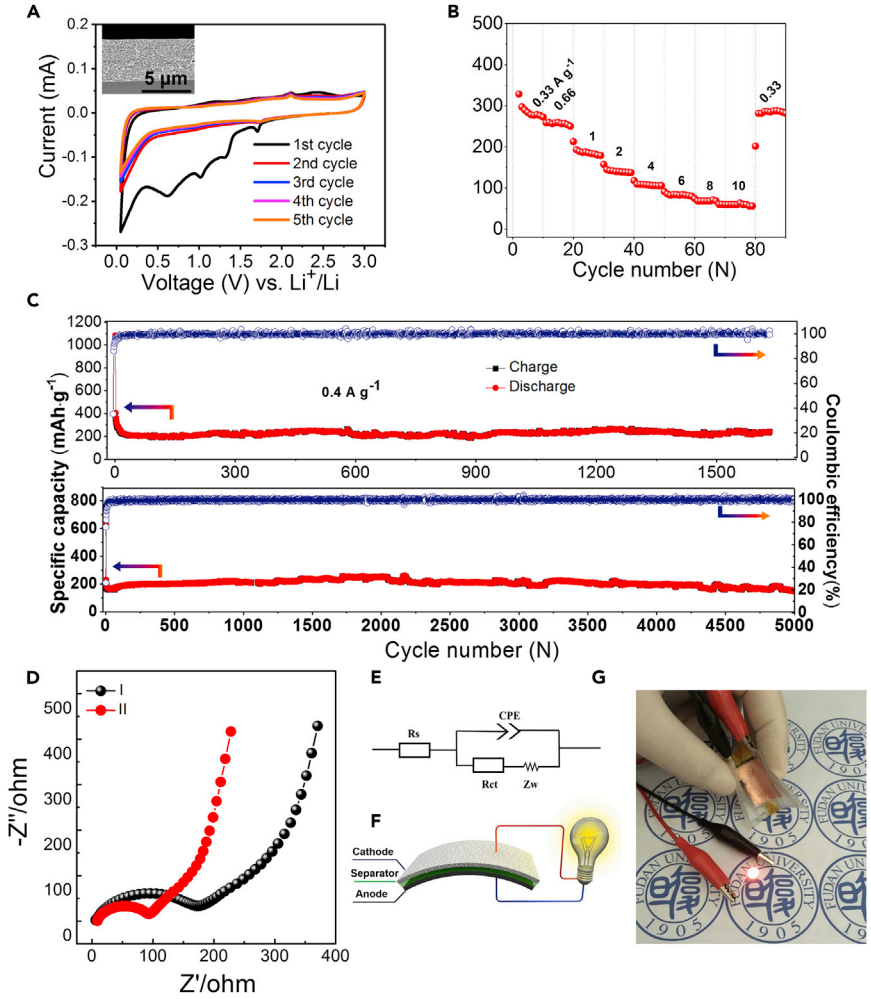

Figure 3. Electrochemical Performances

(A) Cyclic voltammograms of the mesoporous TiO_2/TiC@C composite membrane electrode in a voltage range of 0.01–3 V at a scanning rate of 1 mV•s^{-1} and the corresponding cross-section scanning electron microscopic image (inset).

(B) Rate performance of the mesoporous TiO_2/TiC@C composite membrane electrodes.

(C) Cycling performance of the mesoporous TiO_2/TiC@C composite membrane electrodes at current densities of 0.4 and 1.5 A•g^{-1}.

(D) Nyquist plots of the mesoporous composite membrane electrodes: (I) TiO_2@C and (II) TiO_2/TiC@C.

(E) Equivalent circuit of the mesoporous TiO_2/TiC@C composite membrane electrodes.

(F) Schematic diagram of a flexible full battery.

(G) Photograph of a red LED lightened by the flexible battery under bending. See also Figures S15–S26 and Table S2.

carbon electrode after 1,000 cycles, where the ordered mesopores are totally distorted or even collapsed (Figure S28). However, it is found that the structure of the mesoporous TiO_2/TiC@C composite membrane can still be well retained after 1,600 cycles. The TiO_2 nanocrystals and TiC nanodots with a thin SEI film and size less than 5 nm are still dispersed uniformly in the mesoporous carbon matrix (Figures 5B and S29), which is almost the same as that before the cycling.

Mechanics Simulations

To deeply understand the origin of the anti-collapse property of the TiO_2/TiC@C membrane electrode during the lithiation process, a simulation of elastic-plastic evolution coupled to Li diffusion was adopted to evaluate the lithiation-induced deformation and stress states. The simulated results for the TiO_2@C and TiO_2/TiC@C composites are shown (Figure 6). It should be noted that our diffusion simulations mainly serve

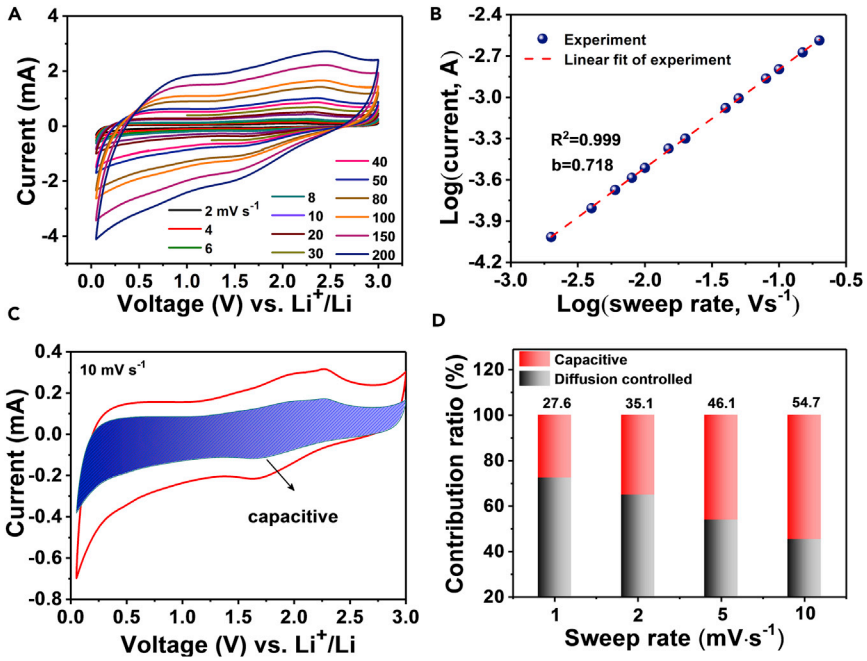

Figure 4. Electrochemical Kinetics Analysis

(A) CV curves at various scan rates from 2 to 200 mV s^{-1} of the mesoporous TiO_2/TiC@C composite membrane electrodes.

(B) Log(*i*) versus log (*v*) plots of the cathodic current response at ~ 2.05 V of the mesoporous TiO_2/TiC@C membrane electrodes.

(C) Separation of the capacitive and diffusion currents in the mesoporous TiO_2/TiC@C composite membrane electrodes at a scan rate of 10 mV s^{-1}.

(D) Contribution ratio of the capacitive and diffusion-controlled charge versus scan rate. See also Figures S27 and S28.

to generate the deformation of the structures for the stress analyses, rather than provide a precise description of the dynamic lithiation process. The configurations of the TiO_2@C and TiO_2/TiC@C composites for simulations and stress evolution during lithiation process are shown (Figure 6A). The regions filled with different colors from blue to red signify different stress states of tensile stresses (quantitated with positive values) and compressive stresses (quantitated with negative values) (Figure 6B). The green region means stress-free state, the red region means high-magnitude tensile stress, and the colors between green and red regions are the stress-excessive boundary. Similarly, the blue region means high-magnitude compressive stress and the colors between green and blue regions are the stress-excessive boundary. During the process of lithiation, inside channels are filled with a constant Li-ion concentration and subjected to an invariant lithium flux (J_0) inside the channels. The stress simulation (Figure 6C) reveals that, after the lithiation of the TiO_2/TiC@C composite, when the state of charge value (*SOC*) (*SOC* = 0 represents the lithium-free state, and *SOC* = 1, the fully lithiated state) ranges from 0 to 0.1, a hoop maximum tensile stress (~9.7 MPa) drastically generates at the TiO_2-C interface. For the TiO_2@C composite, a similar structural deformation occurs during lithiation. However, the maximum hoop tensile stress generated at the TiO_2-C interface is ~31.1 MPa, three times that of the TiO_2-C interface of TiO_2/TiC@C composite, which may lead to the structure collapse of the TiO_2@C composite at the very beginning of the lithiation process. It is noted that when the *SOC* value is in the range of 0.1–0.4, the TiO_2-C interface of the TiO_2@C composite undergoes a higher maximum radial tensile stress (~39.5 MPa) than that (~11.5 MPa) of the TiO_2-C interface of TiO_2/TiC@C composite (Figure 6D), clearly demonstrating that the TiO_2/TiC@C composite possesses higher structural stability due to the stable TiO_2-C interface.

DISCUSSION

On the basis of substantial data and discussion, the possible mechanism for superior lithium storage performance over the mesoporous TiO_2/TiC@C composite membrane electrodes has been proposed (Figure 5C). The stiff TiC nanodots attached on the surface of TiO_2 nanocrystals can effectively avoid the

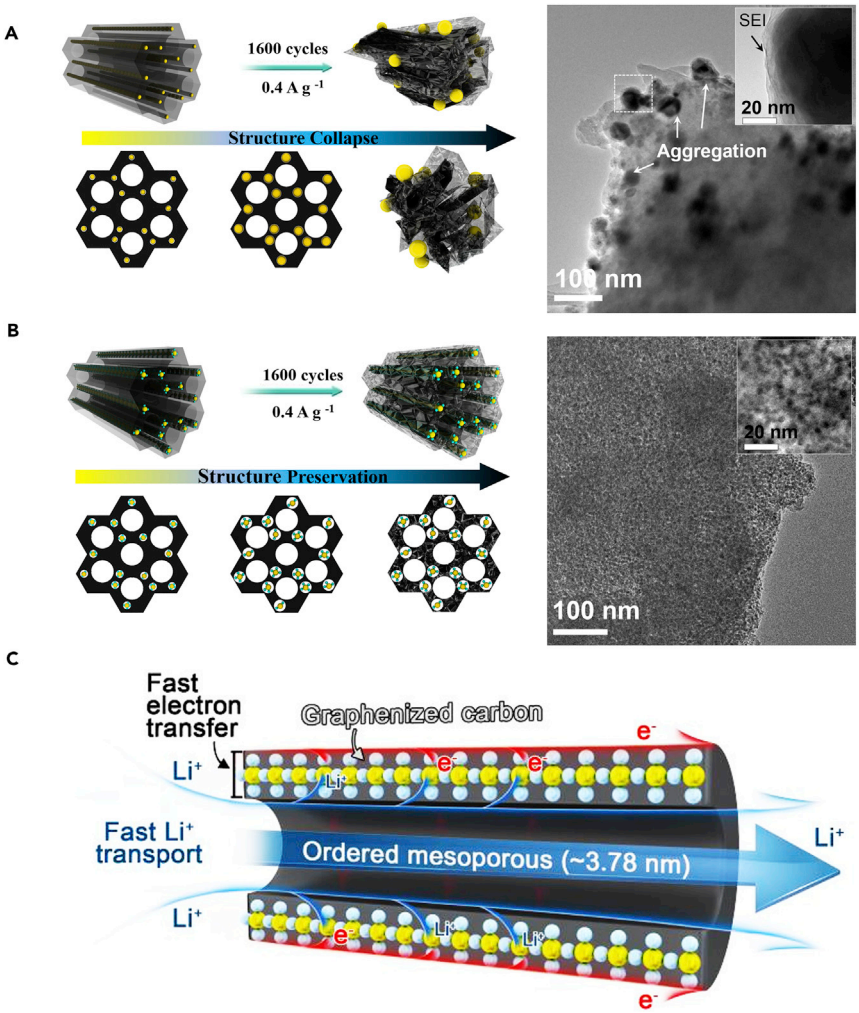

Figure 5. Structural Evolution and Lithium Storage Mechanism

(A) Schematic illustrations of the structural evolution of mesoporous TiO_2@C composite membrane electrodes upon cycling and the corresponding TEM image.

(B) Schematic illustrations of the structural evolution of the mesoporous TiO_2/TiC@C composite membrane electrodes upon cycling and the corresponding TEM image.

(C) Charge-discharge mechanism for the mesoporous TiO_2/TiC@C composite membrane electrodes as the high-performance lithium battery. See also Figure S29.

aggregation of TiO_2 nanocrystals and prevent the collapse of the composite frameworks, which provide a stable TiO_2-C interface to withstand lithium-ion insertion and extraction, thus enabling a stable cycling performance. On the other hand, the highly conductive TiC nanodots serve as a bridge between the TiO_2 nanocrystals and mesoporous carbon matrix to facilitate electron transfer, which is conducive to forming a thickness-reduced SEI film on the surface of the TiO_2 nanocrystals, giving rise to an improved rate performance. Furthermore, the mesoporous structure of the membranes offers direct and short pathways for lithium-ion diffusion and electrolyte penetration, beneficial for fast and robust lithium storage. Accordingly, the mesoporous TiO_2/TiC@C composite membranes exhibit outstanding lithium storage performance, such as high capacity, superior high-rate capability, and long cycling stability. Moreover, a flexible full battery can be assembled by using the TiO_2/TiC@C membrane as an anode, highlighting the great potentials of the composite membranes in practical energy applications such as portable bendable electronics and flexible energy storage devices. We expect that this work can open an avenue to constructing interface-stable composite structures by introducing transition metal carbide nanodots with electrochemical inactivity and conductivity for the development of new-generation LIBs with both high power and long cycling life.

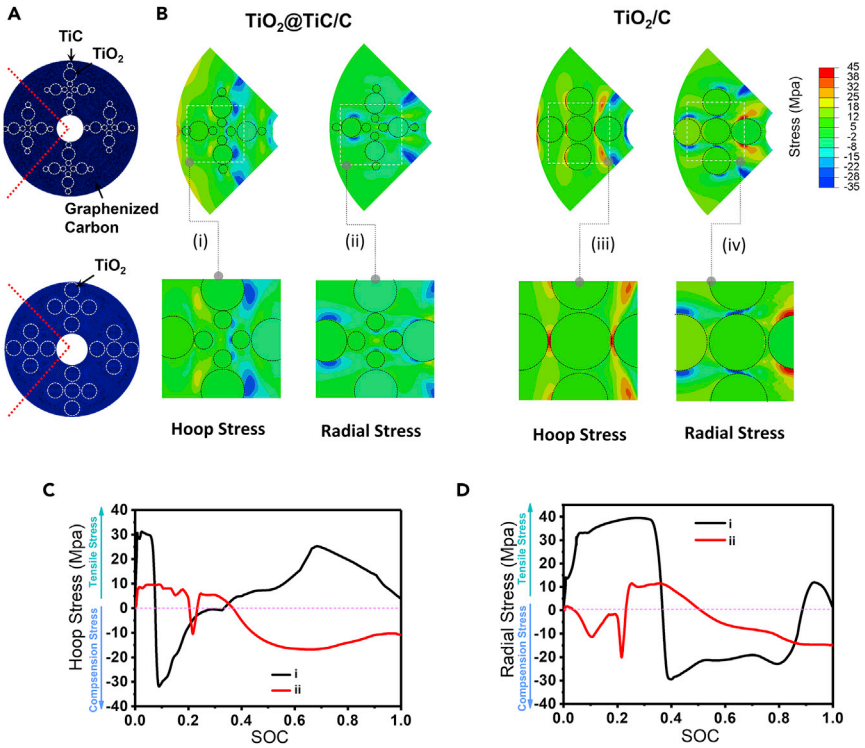

Figure 6. Mechanics Simulations

(A) Finite element simulations model of the mesoporous TiO_2@C and TiO_2/TiC@C models.

(B) Stress distributions from finite element simulations of quarter of the mesoporous carbon frameworks during lithiation process. The steps (i) and (ii) and (iii) and (iv) correspond to radial and hoop stress values for the two mesoporous composites, respectively. Top panels depict the quarter of mesoporous carbon framework; bottom panels are enlarged views of the regions marked by rectangles in (i)–(iv).

(C and D) Evolution of hoop (C) and radial stress (D) in the TiO_2@C (I, black curve) and TiO_2/TiC@C (II, red curve) composites after lithiation.

METHODS

All methods can be found in the accompanying Transparent Methods supplemental file.

SUPPLEMENTAL INFORMATION

Supplemental Information includes Transparent Methods, 29 figures, 3 tables, and 1 video and can be found with this article online at https://doi.org/10.1016/j.isci.2018.04.009.

ACKNOWLEDGMENTS

This work was supported by the State Key Basic Research Program of the PRC (2012CB224805, 2013CB934104, and 2017YFA0207300), Shanghai Science and Technology Committee (14JC1400700), NSF of China (Grant Nos. 21210004, 21603036, and 21273161), the Natural Science Foundation of Shanghai (Grant No. 17ZR1447800), the Program for Professor of Special Appointment (Eastern Scholar) at Shanghai Institutions of Higher Learning, Hundred Youth Talent Plan of Tongji University, and the Fundamental Research Funds for the Central Universities.

AUTHOR CONTRIBUTIONS

D.Z proposed and supervised the project. W.Z., L.Z., J.Y. and D.Z. conceived the study and co-wrote the manuscript. W.Z. and L.Z carried out the synthesis and electrochemical evaluation. B.C. and L.Z. preformed the mechanics simulations. B.K., H.H., K.L., and Y.L. helped with material characterization and manuscript preparation. All authors discussed the results and commented on the manuscript.

DECLARATION OF INTERESTS

The authors declare no conflict of interests.

Received: December 8, 2017
Revised: March 20, 2018
Accepted: March 27, 2018
Published: May 25, 2018

REFERENCES

Allcorn, E., and Manthiram, A. (2015). High-rate, high-density FeSb–TiC–C nanocomposite anodes for lithium-ion batteries. J. Mater. Chem. A *3*, 3891–3900.

Angelomé, P.C., Andrini, L., Calvo, M.E., Requejo, F.G., Bilmes, S.A., and Soler-Illia, G.J. (2007). Mesoporous anatase TiO_2 films: use of Ti K XANES for the quantification of the nanocrystalline character and substrate effects in the photocatalysis behavior. J. Phys. Chem. C *111*, 10886–10893.

Aricò, A.S., Bruce, P., Scrosati, B., Tarascon, J.-M., and Van Schalkwijk, W. (2005). Nanostructured materials for advanced energy conversion and storage devices. Nat. Mater. *4*, 366–377.

Armand, M., and Tarascon, J.-M. (2008). Building better batteries. Nature *451*, 652–657.

Armstrong, G., Armstrong, A.R., Bruce, P.G., Reale, P., and Scrosati, B. (2006). TiO_2(B) nanowires as an improved anode material for lithium-ion batteries containing $LiFePO_4$ or $LiNi_{0.5}Mn_{1.5}O_4$ cathodes and a polymer electrolyte. Adv. Mater. *18*, 2597–2600.

Augustyn, V., Come, J., Lowe, M.A., Kim, J.W., Taberna, P.-L., Tolbert, S.H., Abruña, H.D., Simon, P., and Dunn, B. (2013). High-rate electrochemical energy storage through Li^+ intercalation pseudocapacitance. Nat. Mater. *12*, 518–522.

Cai, Z., Xu, L., Yan, M., Han, C., He, L., Hercule, K.M., Niu, C., Yuan, Z., Xu, W., and Qu, L. (2014). Manganese oxide/carbon yolk–shell nanorod anodes for high capacity lithium batteries. Nano Lett. *15*, 738–744.

Fang, Y., Lv, Y., Che, R., Wu, H., Zhang, X., Gu, D., Zheng, G., and Zhao, D. (2013). Two-dimensional mesoporous carbon nanosheets and their derived graphene nanosheets: synthesis and efficient lithium ion storage. J. Am. Chem. Soc. *135*, 1524–1530.

Fang, Y., Lv, Y., Gong, F., Elzatahry, A.A., Zheng, G., and Zhao, D. (2016). Synthesis of 2D-mesoporous-carbon/MoS_2 heterostructures with well-defined interfaces for high-performance lithium-ion batteries. Adv. Mater. *28*, 9385–9390.

Feng, D., Lv, Y., Wu, Z., Dou, Y., Han, L., Sun, Z., Xia, Y., Zheng, G., and Zhao, D. (2011). Free-standing mesoporous carbon thin films with highly ordered pore architectures for nanodevices. J. Am. Chem. Soc. *133*, 15148–15156.

Gu, D., Li, W., Wang, F., Bongard, H., Spliethoff, B., Schmidt, W., Weidenthaler, C., Xia, Y., Zhao, D., and Schüth, F. (2015). Controllable synthesis of mesoporous peapod-like Co_3O_4@carbon nanotube arrays for high-performance lithium-ion batteries. Angew. Chem. Int. Ed. *54*, 7060–7064.

Guan, B.Y., Yu, L., Li, J., and Lou, X.W.D. (2016). A universal cooperative assembly-directed method for coating of mesoporous TiO_2 nanoshells with enhanced lithium storage properties. Sci. Adv. *2*, e1501554.

Huang, C.-H., Gu, D., Zhao, D., and Doong, R.-A. (2010). Direct synthesis of controllable microstructures of thermally stable and ordered mesoporous crystalline titanium oxides and carbide/carbon composites. Chem. Mater. *22*, 1760–1767.

Huang, H.-B., Yang, Y., Chen, L.-H., Wang, Y., Huang, S.-Z., Tao, J.-W., Ma, X.-T., Hasan, T., Li, Y., and Xu, Y. (2016). Hierarchical TiO_2/C nanocomposite monoliths with a robust scaffolding architecture, mesopore–macropore network and TiO_2–C heterostructure for high-performance lithium ion batteries. Nanoscale *8*, 10928–10937.

Jeong, J.M., Choi, B.G., Lee, S.C., Lee, K.G., Chang, S.J., Han, Y.K., Lee, Y.B., Lee, H.U., Kwon, S., and Lee, G. (2013). Hierarchical hollow spheres of Fe_2O_3@ polyaniline for lithium ion battery anodes. Adv. Mater. *25*, 6250–6255.

Kaskhedikar, N.A., and Maier, J. (2009). Lithium storage in carbon nanostructures. Adv. Mater. *21*, 2664–2680.

Kim, J.H., Zhu, K., Yan, Y., Perkins, C.L., and Frank, A.J. (2010). Microstructure and pseudocapacitive properties of electrodes constructed of oriented NiO-TiO_2 nanotube arrays. Nano Lett. *10*, 4099–4104.

Kiran, V., and Sampath, S. (2012). Enhanced Raman spectroscopy of molecules adsorbed on carbon-doped TiO_2 obtained from titanium carbide: a visible-light-assisted renewable substrate. ACS Appl. Mater. Interfaces *4*, 3818–3828.

Kong, B., Zu, L., Peng, C., Zhang, Y., Zhang, W., Tang, J., Selomulya, C., Zhang, L., Chen, H., and Wang, Y. (2016). Direct superassemblies of freestanding metal–carbon frameworks featuring reversible crystalline-phase transformation for electrochemical sodium storage. J. Am. Chem. Soc. *138*, 16533–16541.

Larcher, D., and Tarascon, J.-M. (2015). Towards greener and more sustainable batteries for electrical energy storage. Nat. Chem. *7*, 19–29.

Liu, L., and Chen, X. (2014). Titanium dioxide nanomaterials: self-structural modifications. Chem. Rev. *114*, 9890–9918.

Liu, Y., Luo, Y., Elzatahry, A.A., Luo, W., Che, R., Fan, J., Lan, K., Al-Enizi, A.M., Sun, Z., and Li, B. (2015a). Mesoporous TiO_2 mesocrystals: remarkable defects-induced crystallite-interface reactivity and their in situ conversion to single crystals. ACS Cent. Sci. *1*, 400–408.

Liu, H., Li, W., Shen, D., Zhao, D., and Wang, G. (2015b). Graphitic carbon conformal coating of mesoporous TiO_2 hollow spheres for high-performance lithium ion battery anodes. J. Am. Chem. Soc. *137*, 13161–13166.

Liu, Y., Elzatahry, A.A., Luo, W., Lan, K., Zhang, P., Fan, J., Wei, Y., Wang, C., Deng, Y., and Zheng, G. (2016). Surfactant-templating strategy for ultrathin mesoporous TiO_2 coating on flexible graphitized carbon supports for high-performance lithium-ion battery. Nano Energy *25*, 80–90.

Mo, R., Rooney, D., Sun, K., and Yang, H.Y. (2017). 3D nitrogen-doped graphene foam with encapsulated germanium/nitrogen-doped graphene yolk-shell nanoarchitecture for high-performance flexible Li-ion battery. Nat. Commun. *8*, 13949.

Peng, C., Chen, B., Qin, Y., Yang, S., Li, C., Zuo, Y., Liu, S., and Yang, J. (2012). Facile ultrasonic synthesis of CoO quantum dot/graphene nanosheet composites with high lithium storage capacity. ACS Nano *6*, 1074–1081.

Peng, H.J., Zhang, G., Chen, X., Zhang, Z.W., Xu, W.T., Huang, J.Q., and Zhang, Q. (2016). Enhanced electrochemical kinetics on conductive polar mediators for lithium–sulfur batteries. Angew. Chem. Int. Ed. *55*, 12990–12995.

Shan, Z., Archana, P.S., Shen, G., Gupta, A., Bakker, M.G., and Pan, S. (2015). NanoCOT: low-cost nanostructured electrode containing carbon, oxygen, and titanium for efficient oxygen evolution reaction. J. Am. Chem. Soc. *137*, 11996–12005.

Su, Q., Xie, D., Zhang, J., Du, G., and Xu, B. (2013). In situ transmission electron microscopy observation of the conversion mechanism of Fe_2O_3/graphene anode during lithiation–delithiation processes. ACS Nano *7*, 9115–9121.

Wang, J., Yang, N., Tang, H., Dong, Z., Jin, Q., Yang, M., Kisailus, D., Zhao, H., Tang, Z., and Wang, D. (2013). Accurate control of multishelled Co_3O_4 hollow microspheres as high-performance anode materials in lithium-ion batteries. Angew. Chem. Int. Ed. *52*, 6417–6420.

Wang, D., Yu, Y., He, H., Wang, J., Zhou, W., and Abruna, H.D. (2015). Template-free synthesis of hollow-structured Co_3O_4 nanoparticles as

high-performance anodes for lithium-ion batteries. ACS Nano *9*, 1775–1781.

Wang, Y., Yu, L., and Lou, X.W.D. (2016a). Formation of triple-shelled molybdenum–polydopamine hollow spheres and their conversion into MoO_2/carbon composite hollow spheres for lithium-ion batteries. Angew. Chem. Int. Ed. *55*, 14668–14672.

Wang, H., Zhang, Y., Ang, H., Zhang, Y., Tan, H.T., Zhang, Y., Guo, Y., Franklin, J.B., Wu, X.L., and Srinivasan, M. (2016b). A high-energy lithium-ion capacitor by integration of a 3D interconnected titanium carbide nanoparticle chain anode with a pyridine-derived porous nitrogen-doped carbon cathode. Adv. Funct. Mater. *26*, 3082–3093.

Yao, Y., Huo, K., Hu, L., Liu, N., Cha, J.J., McDowell, M.T., Chu, P.K., and Cui, Y. (2011). Highly conductive, mechanically robust, and electrochemically inactive TiC/C nanofiber scaffold for high-performance silicon anode batteries. ACS Nano *5*, 8346–8351.

Yu, T., Deng, Y., Wang, L., Liu, R., Zhang, L., Tu, B., and Zhao, D. (2007). Ordered mesoporous nanocrystalline titanium-carbide/carbon composites from in situ carbothermal reduction. Adv. Mater. *19*, 2301–2306.

Yu, L., Wu, H.B., and Lou, X.W.D. (2017a). Self-templated formation of hollow structures for electrochemical energy applications. Acc. Chem. Res. *50*, 293–301.

Yu, L., Hu, H., Wu, H.B., and Lou, X.W.D. (2017b). Complex hollow nanostructures: synthesis and energy-related applications. Adv. Mater. https://doi.org/10.1002/adma.201604563.

Zeng, L., Zheng, C., Xia, L., Wang, Y., and Wei, M. (2013). Ordered mesoporous TiO_2–C nanocomposite as an anode material for long-term performance lithium-ion batteries. J. Mater. Chem. A *1*, 4293–4299.

Zhang, R., Elzatahry, A.A., Al-Deyab, S.S., and Zhao, D. (2012). Mesoporous titania: from synthesis to application. Nano Today *7*, 344–366.

Zhang, R., Du, Y., Li, D., Shen, D., Yang, J., Guo, Z., Liu, H.K., Elzatahry, A.A., and Zhao, D. (2014). Highly reversible and large lithium storage in mesoporous Si/C nanocomposite anodes with silicon nanoparticles embedded in a carbon framework. Adv. Mater. *26*, 6749–6755.

ISCI, Volume *3*

Supplemental Information

Mesoporous TiO_2/TiC@C Composite Membranes with Stable TiO_2-C Interface for Robust Lithium Storage

Wei Zhang, Lianhai Zu, Biao Kong, Bingjie Chen, Haili He, Kun Lan, Yang Liu, Jinhu Yang, and Dongyuan Zhao

Supplemental Data Items

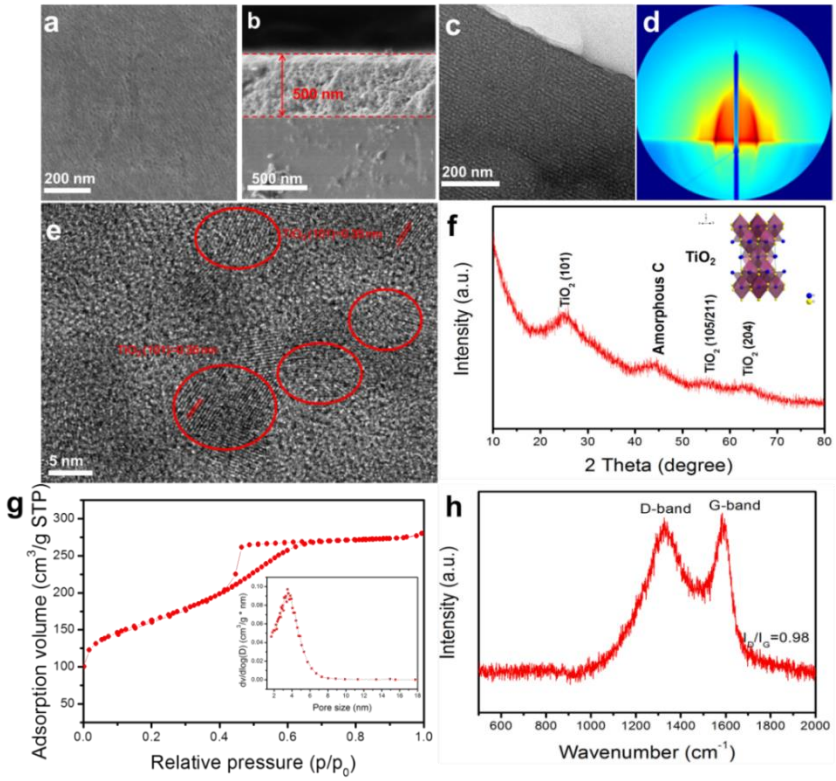

Figure S1. Structure and composition characterizations of the mesoporous TiO_2@C membranes, related to Figure 2.

Top-view SEM image (a), cross-section SEM image (b), low-magnification TEM image (c), GISAXS image (d), high-resolution TEM (HRTEM) image (e), XRD pattern (f), BET analysis (g), and Raman spectrum (h) of the mesoporous TiO_2@C membranes. The inset in (f) shows the molecule structure of TiO_2. The inset in (g) is pore size distribution.

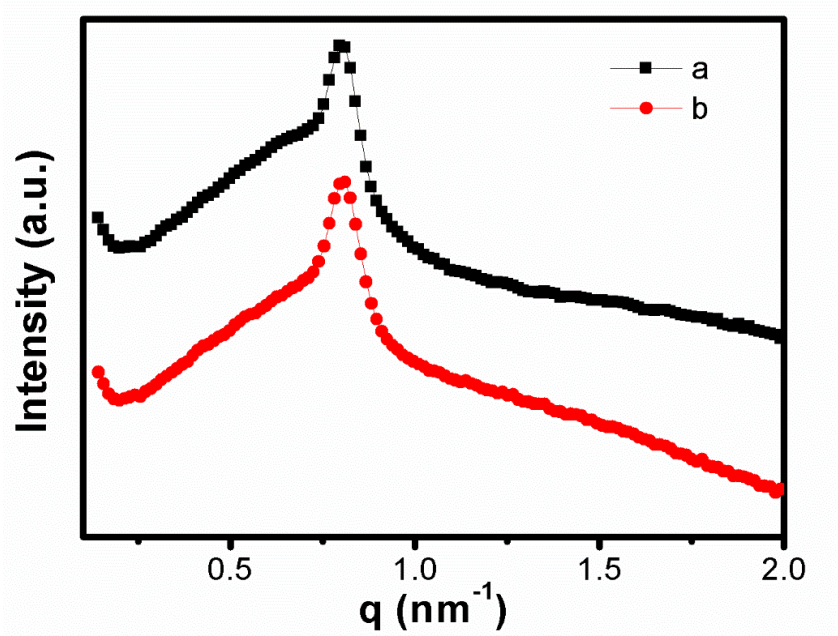

Figure S2. Small angel X-ray diffraction (SAXS), related to Figure 2

SAXS patterns of the mesoporous TiO_2@C (a) and TiO_2/TiC@C (b) membranes.

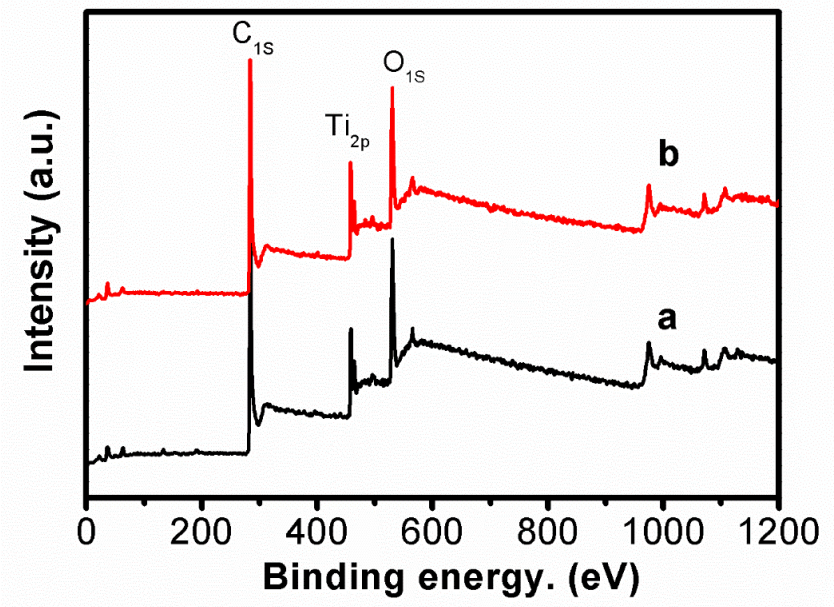

Figure S3. X-ray photoelectron spectroscopy (XPS), related to Figure 2.
XPS spectra of the mesoporous TiO_2@C (a) and TiO_2/TiC@C (b) membranes.

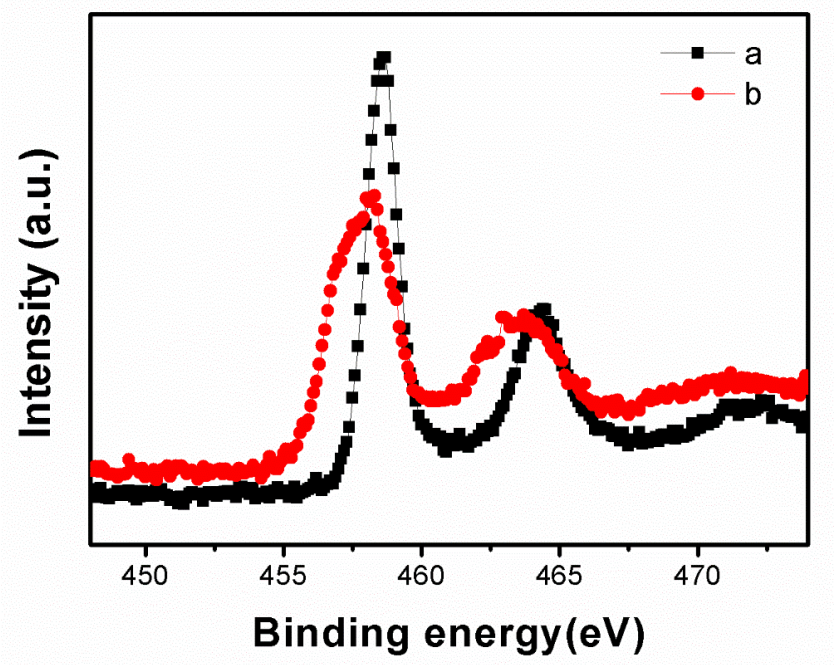

Figure S4. High-resolution XPS spectra, related to Figure 2.
High-resolution XPS spectra of Ti 2p core level for the TiO_2@C (a) and TiO_2/TiC@C (b) membranes.

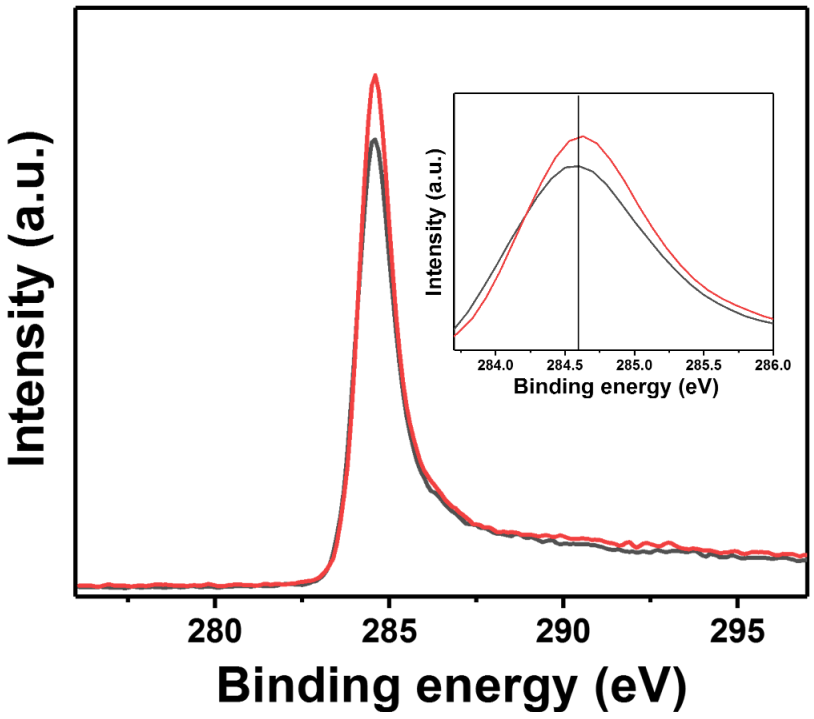

Figure S5. High-resolution XPS spectra, related to Figure 2.

High-resolution XPS spectra of C1s core level for the TiO_2@C (a) and TiO_2/TiC@C (b) membranes.

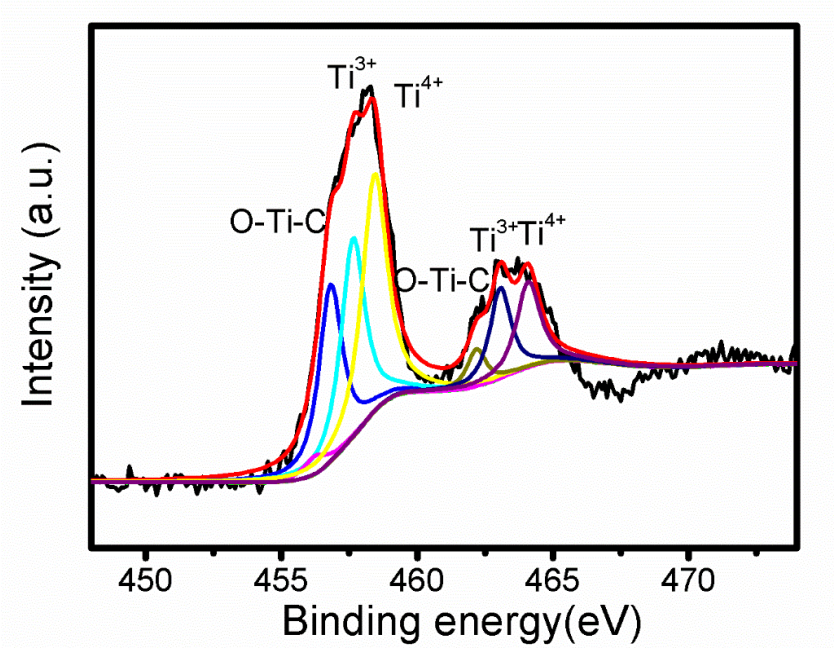

Figure S6. High-resolution XPS spectra, related to Figure 2.

The high-resolution XPS spectrums of Ti 2p core level for the mesoporous TiO_2/TiC@C membranes. The HRXPS contained six components at 456.8, 457.7, 458.5, 462.2, 463.1 and 464.2 eV are consistent with O-Ti-C, Ti^{3+}, Ti^{4+}, O-Ti-C, Ti^{3+}, and Ti^{4+}, respectively.

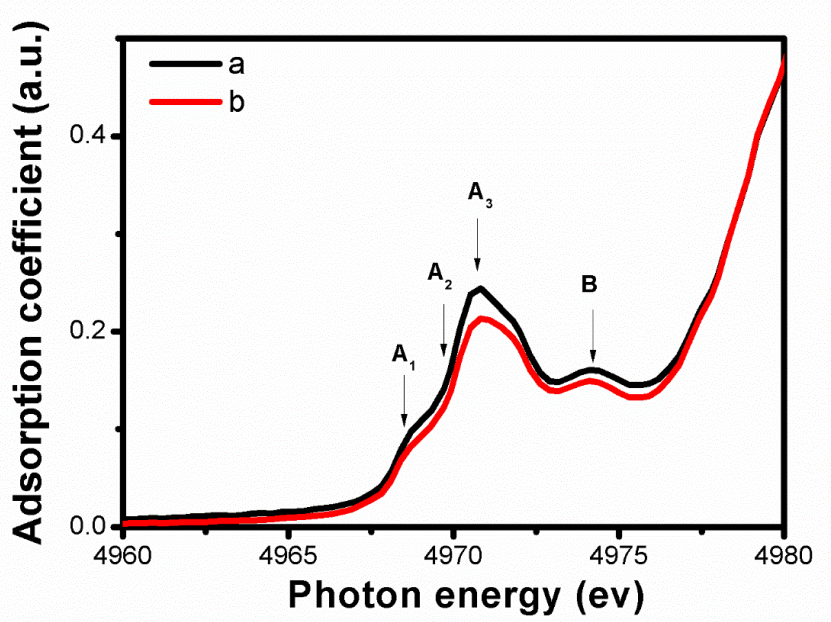

Figure S7. X-ray absorption fine structure spectroscopy (XAFS), related to Figure 2.

The Ti K-edge pre-edge XAFS of the mesoporous TiO_2@C (a) and TiO_2/TiC@C (b) membranes.

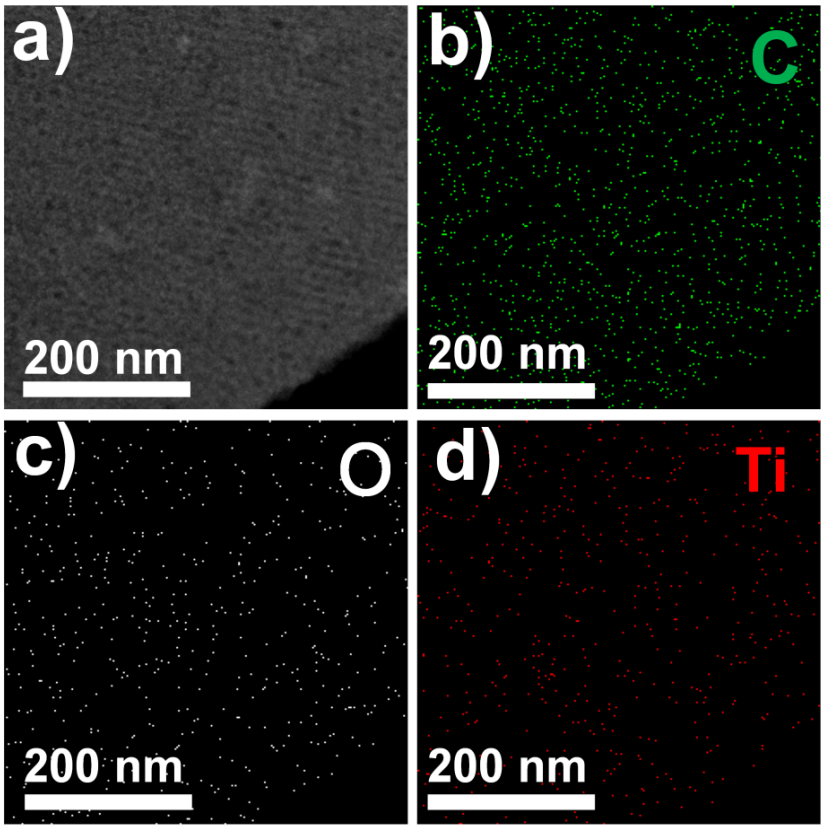

Figure S8. Elemental mapping, related to Figure 2.

The elemental mapping of the mesoporous TiO_2@C membranes. HAADF-STEM (a) image and energy-dispersive X-ray element mapping of C (b), O (c), and Ti (d) elements.

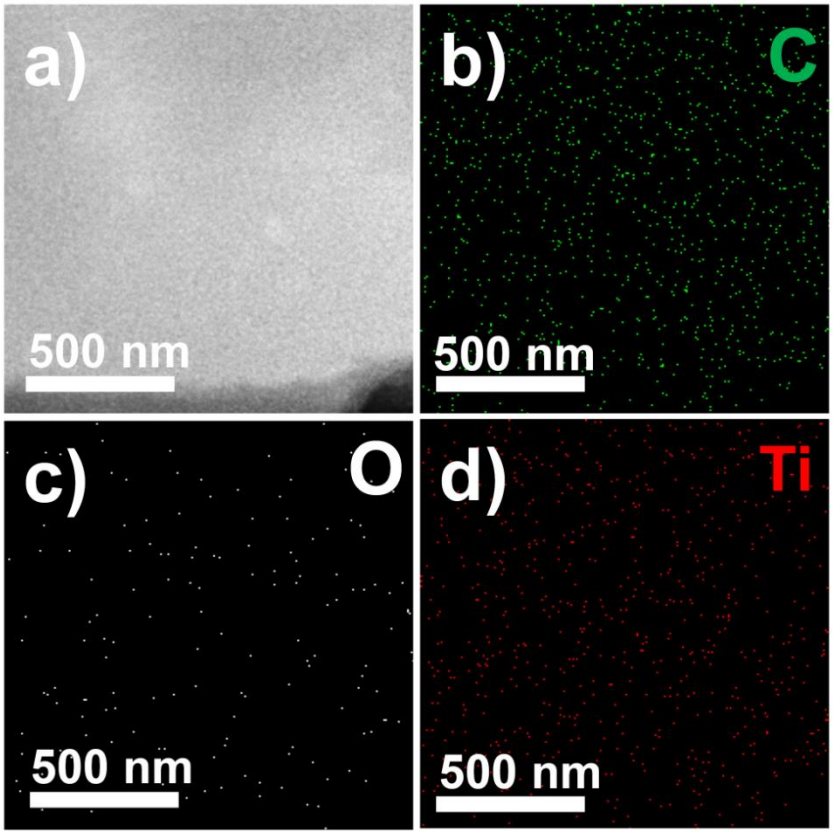

Figure S9. Elemental mapping, related to Figure 2.

The elemental mapping of the mesoporous TiO_2/TiC@C membranes. HAADF-STEM (a) image and energy-dispersive X-ray element mapping of C (b), O (c), and Ti (d) elements.

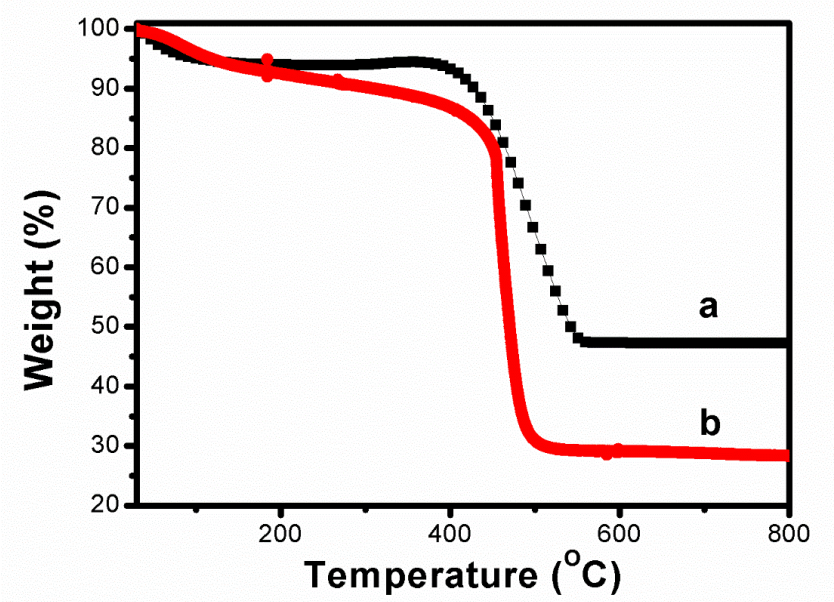

Figure S10.Thermogravimetric analysis, related to Figure 2.

The thermogravimetric analysis curves of the mesoporous TiO_2/TiC@C membranes before (a) and after (b) the removal of TiO_2 nanocrystals by concentrated sulfuric acid.

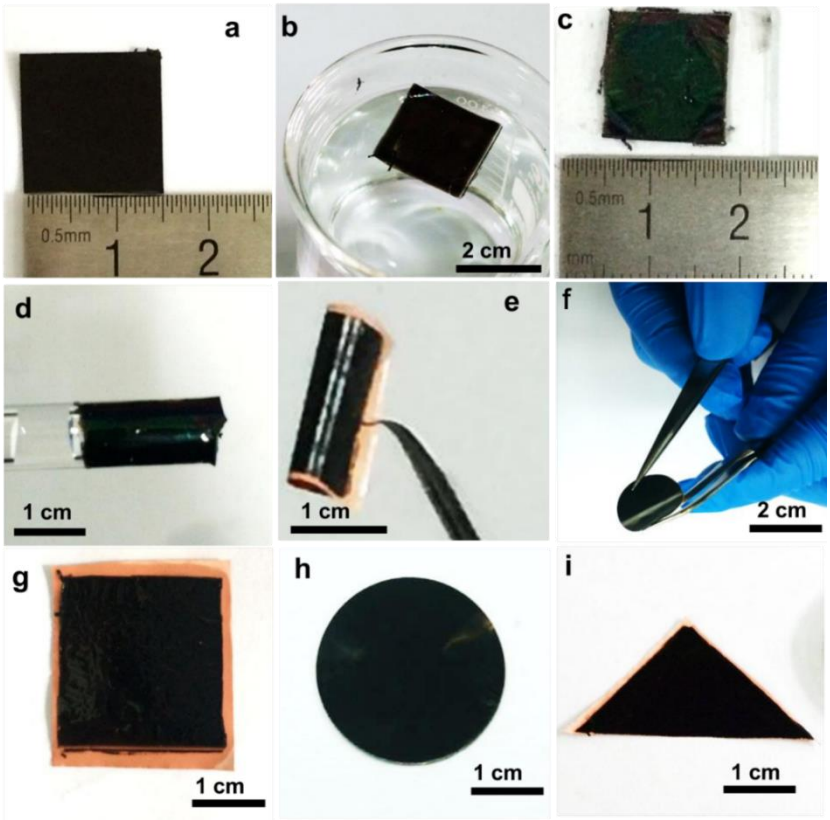

Figure S11. **Transferability, flexibility, tailorability of the mesoporous membranes, related to Figure 2.**

Photographs of the mesoporous TiO_2/TiC@C membranes formed on silicon wafer (a), floating on water (b), transferred onto glass substrate (c), transferred onto a cylindrical substrate (d), bent without cracks (e, d), and tailored to different shapes (g, h, i).

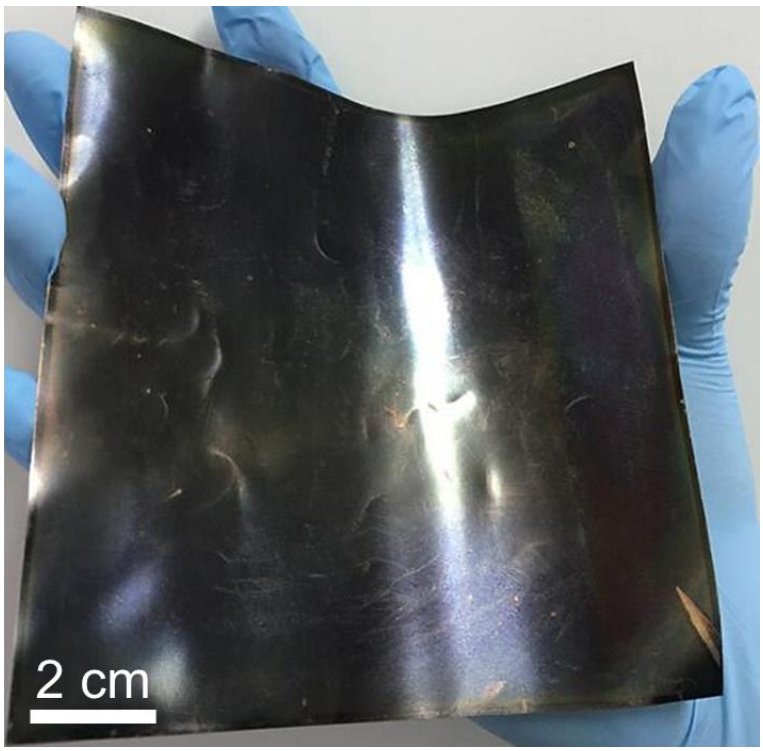

Figure S12. **Processing scalability of the mesoporous membranes, related to Figure 2.**

Photograph of the mesoporous TiO_2/TiC@C membranes formed on a large Ti foil of 144 cm^2.

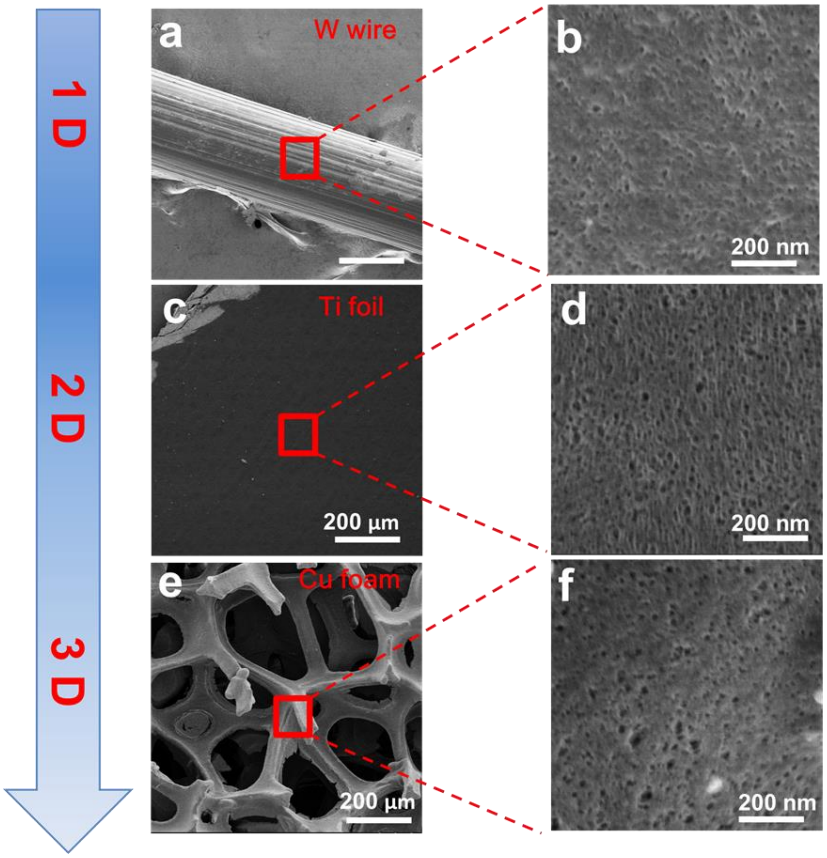

Figure S13. Processing feasibility of the mesoporous membranes, related to Figure 2.

SEM images of mesoporous TiO_2/TiC@C membranes formed on different substrates. (a,b) W wires, (c,d) Ti foils and (e,f) Cu foams.

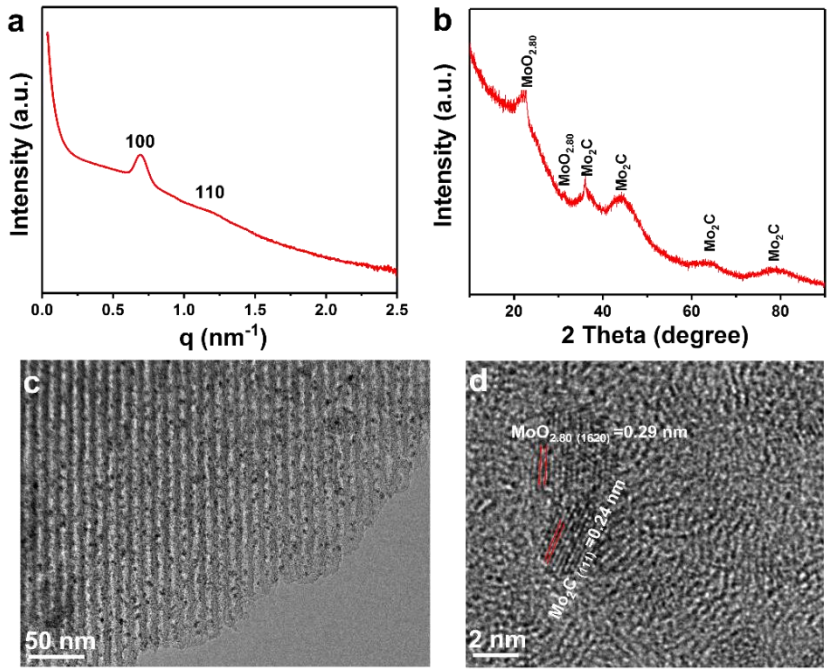

Figure S14. Extension of the synthetic strategy, related to Figure 2.
SAXS (a), XRD (b), TEM (c) and HRTEM (d) images of mesoporous $MoO_{2.80}/Mo_2C$@C composites.

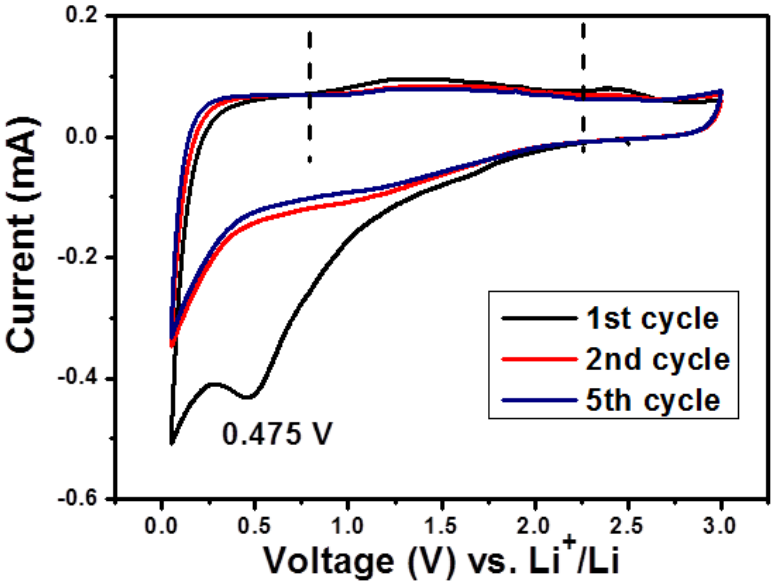

Figure S15. Electrochemical performance of the mesoporous TiO_2@C membranes, related to Figure 3.

Cyclic voltammograms of the mesoporous TiO_2@C membranes electrodes in a voltage range of 0.01–3 V at a scanning rate of 1 $mV \cdot s^{-1}$.

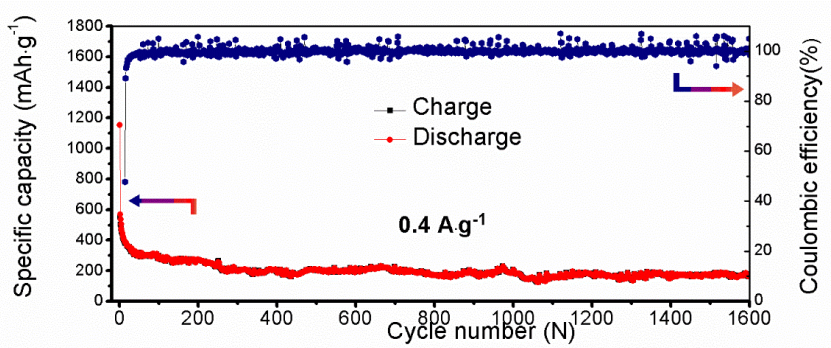

Figure S16. **Electrochemical performance of the mesoporous TiO_2@C membranes, related to Figure 3.**

Cycling performances of the mesoporous TiO_2@C membranes at a current density of 0.4 $A \cdot g^{-1}$.

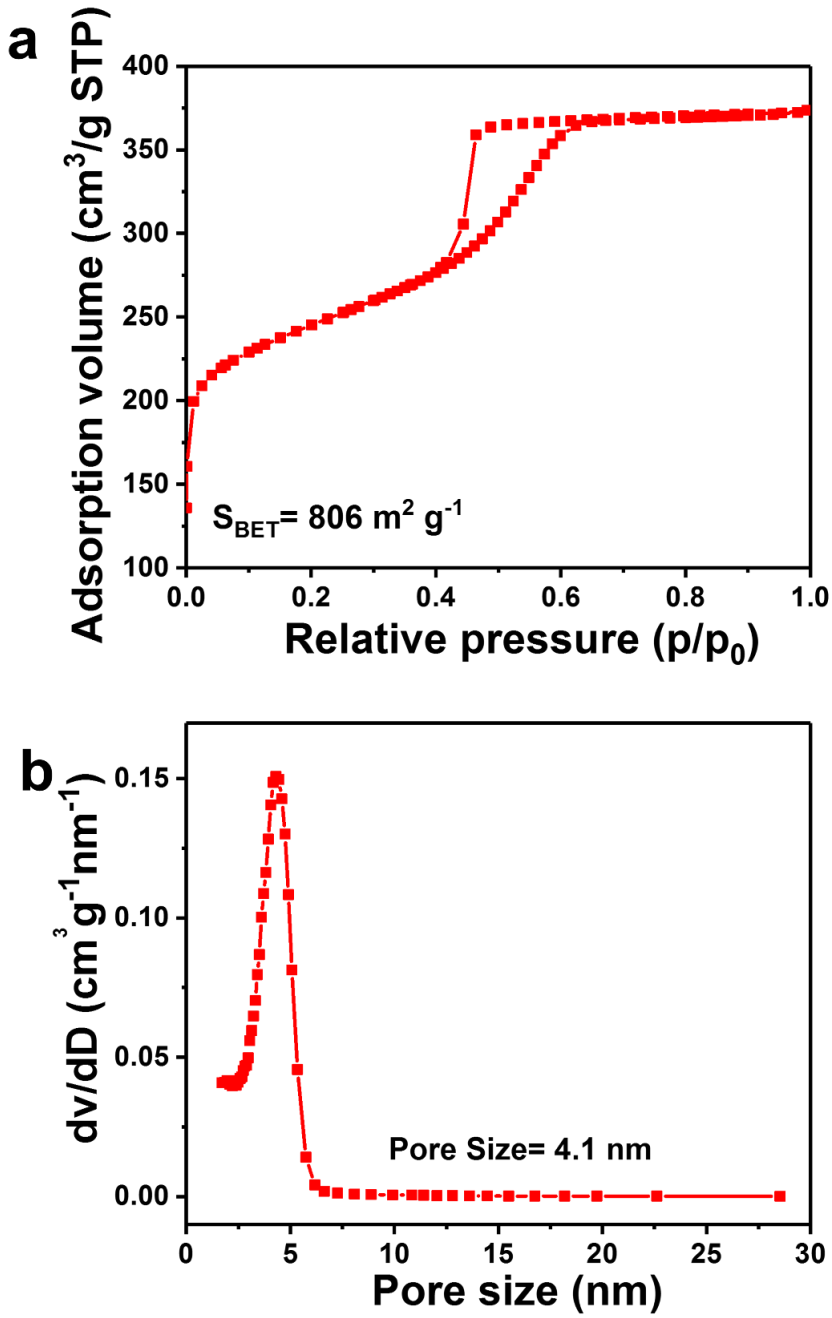

Figure S17. Structure characterizations of the mesoporous carbon, related to Figure 3.

N_2 adsorption-desorption isotherms (a) and the corresponding pore size distribution (b) of the mesoporous carbon annealed at 900 °C.

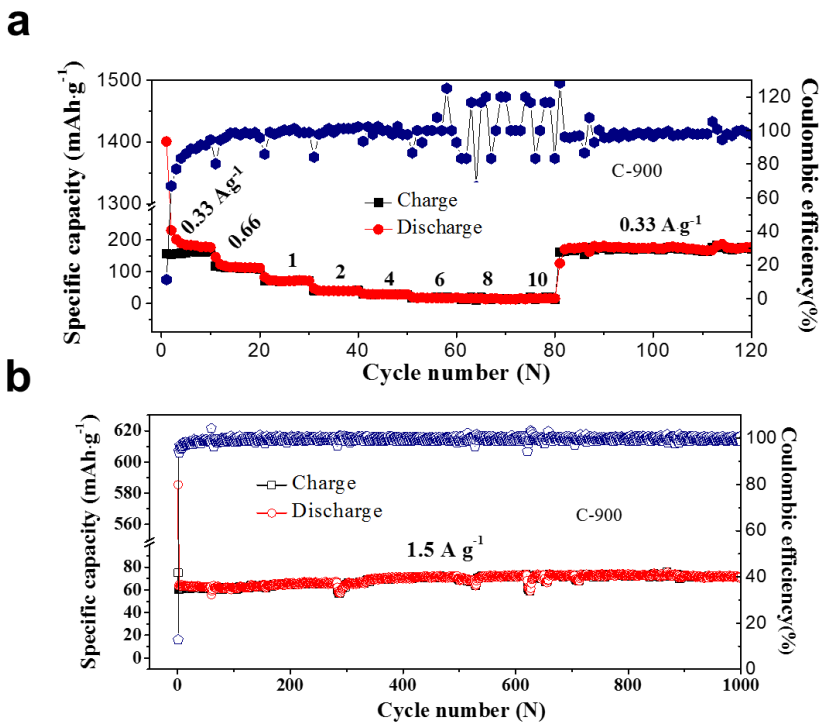

Figure S18. Electrochemical performances of the mesoporous carbon, related to Figure 3.

(a) Rate performance of mesoporous carbon annealed at 900 °C. (b) Cycling performance of mesoporous carbon annealed at 900 °C.

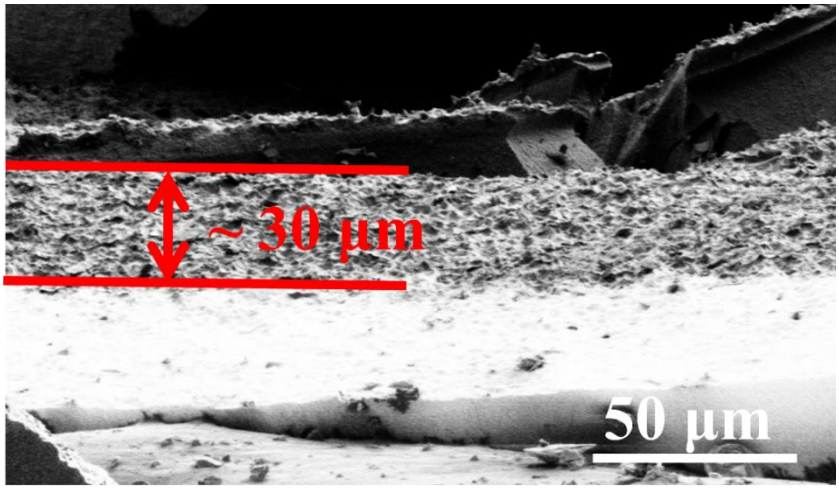

Figure S19. Structure characterizations of the thicker mesoporous TiO_2/TiC@C membrane, related to Figure 3.

Cross-section SEM image of the mesoporous TiO_2/TiC@C membranes with a thickness of ~30 µm synthesized at 100 rpm for 5 s.

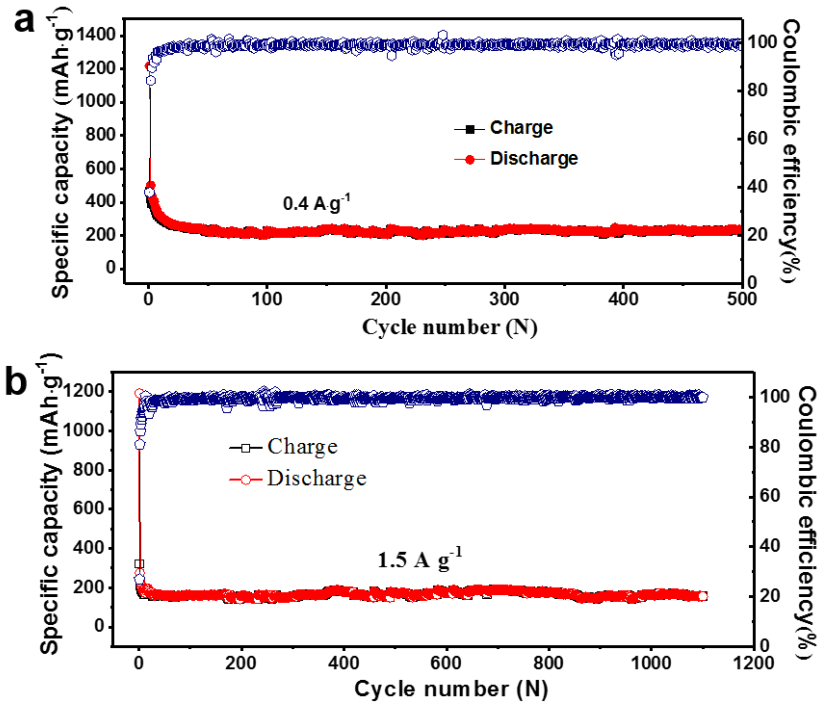

Figure S20. Electrochemical performances of the thicker mesoprous TiO_2/TiC@C membranes, related to Figure 3.

Cycling performance of the mesoporous TiO_2/TiC@C membranes with a thickness of ~ 30 μm at current densities of 0.4 (a) and 1.5 $A \cdot g^{-1}$ (b), respectively.

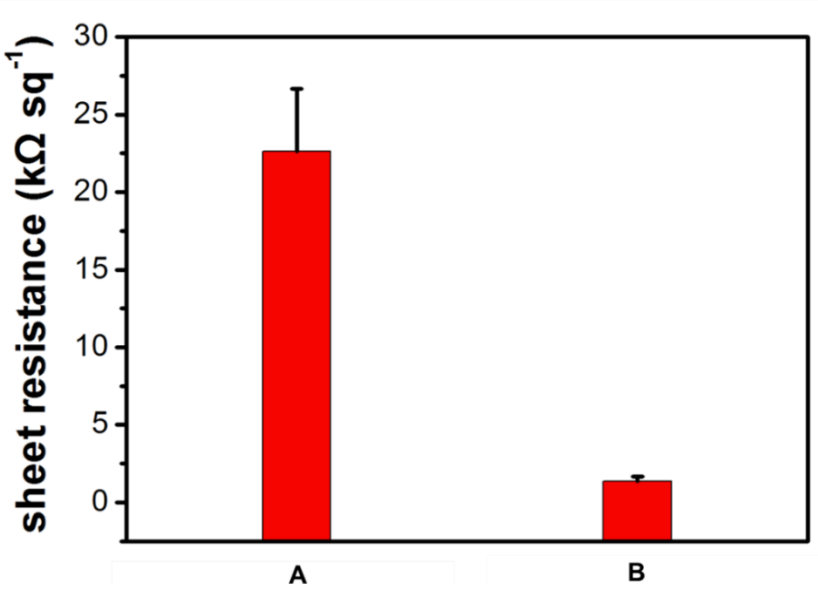

Figure S21. **Sheet resistances, related to Figure 3.**

The sheet resistances of the mesoporous TiO_2@C (A) and TiO_2/TiC@C (B) membranes.

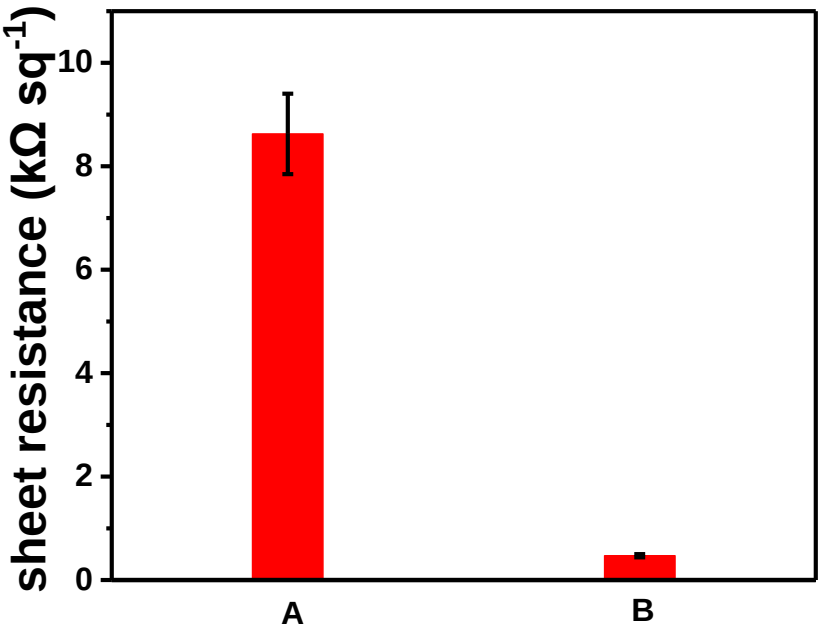

Figure S22. **Sheet resistances, related to Figure 3.**
The sheet resistances of the mesoporous carbon membranes calcination at 700 (A) and 900 °C (B), respectively.

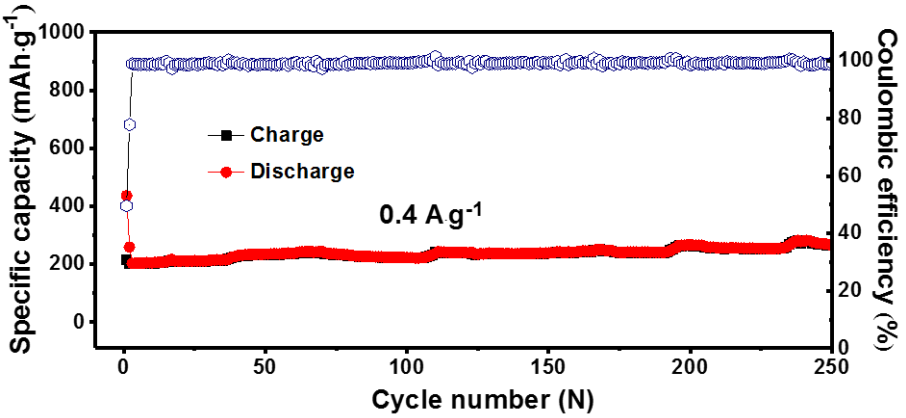

Figure S23. Electrochemical performance of the mesoporous TiO_2/TiC@C membrane after prelithiation, related to Figure 3.

Cycling performance of the mesoporous TiO_2/TiC@C membranes electrodes at current densities of 0.4 $A \cdot g^{-1}$ after prelithiation. The initial coulomb efficiency is increasing from 35.3 to 49.6% after prelithiation.

Figure S24. **Flexible full battery, related to Figure 3.**
Photograph of the flexible full battery assembled by using the TiO_2/TiC@C membranes as the anode (Cu foil as the current collector) and commercial $LiCoO_2$ loaded on Al foil as the cathode.

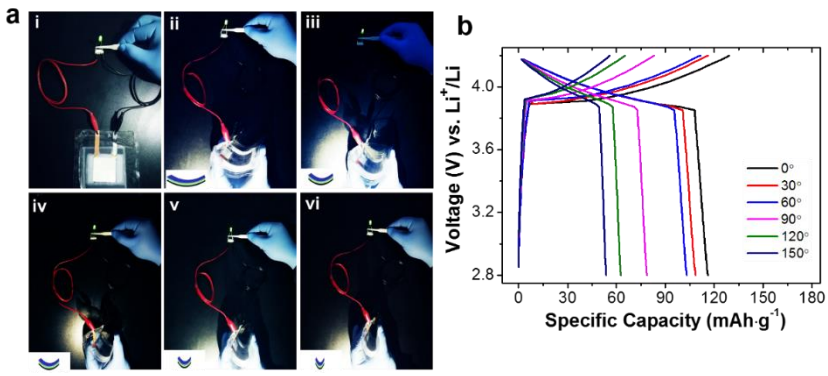

Figure S25. Electrochemical performance of the flexible full battery, related to Figure 3.

(a) Photographs of the flexible full battery with different bent angels and a LED can be stably lit. The bent angle is measured to be 0 (i), 30 (ii), 60 (iii), 90 (iv), 120 (v) and 150°(vi), respectively. (b) Charge/discharge curves of the flexible full battery with different bent.

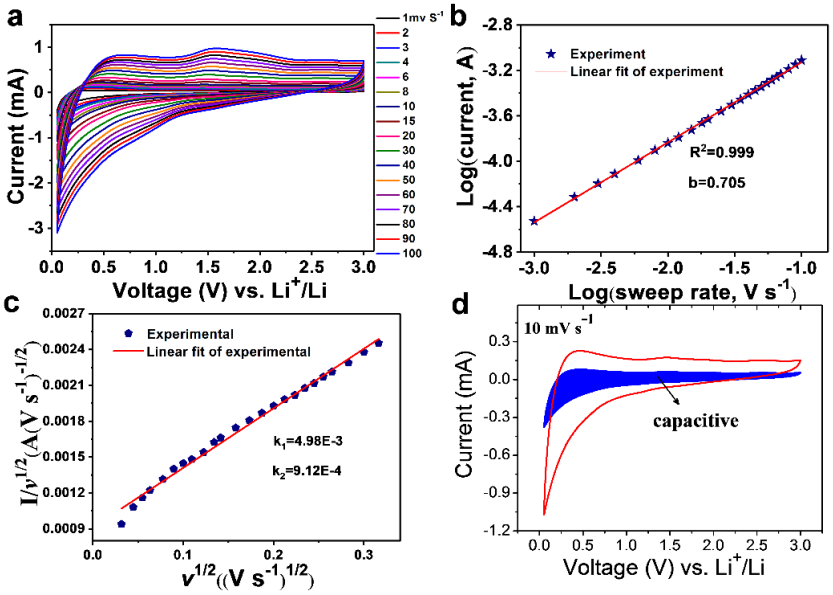

Figure S26. Electrochemical kinetics analysis of the mesoporous carbon, related to Figure 4.

(a) CV curves at various scan rates from 2 to 200 mV s^{-1} of the mesoporous carbon membranes. (b) Log(*i*) vs. log (*v*) plots of the cathodic current response at ~ 2.05 V of the mesoporous carbon membrane electrodes. (c). I/scan $rate^{1/2}$ versus scan $rate^{1/2}$. (d) Separation of the capacitive and diffusion currents in the mesoporous carbon membrane electrodes at a scan rate of 10 mV s^{-1}.

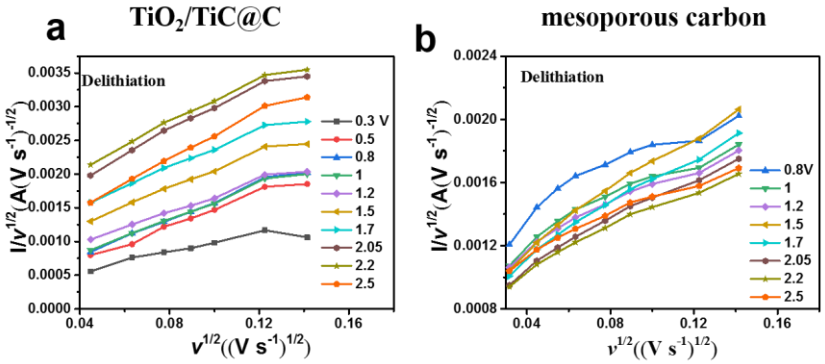

Figure S27. Electrochemical kinetics analysis of the mesoporous carbon and TiO_2/TiC@C c membranes, related to Figure 4.

CV curves of (a) mesoporous carbon, (b) TiO_2/TiC@C membranes at different scan rates, and corresponding plots of $\nu^{1/2}$ vs. $i/\nu^{1/2}$ used for calculating constants k_1 and k_2 at different potentials.

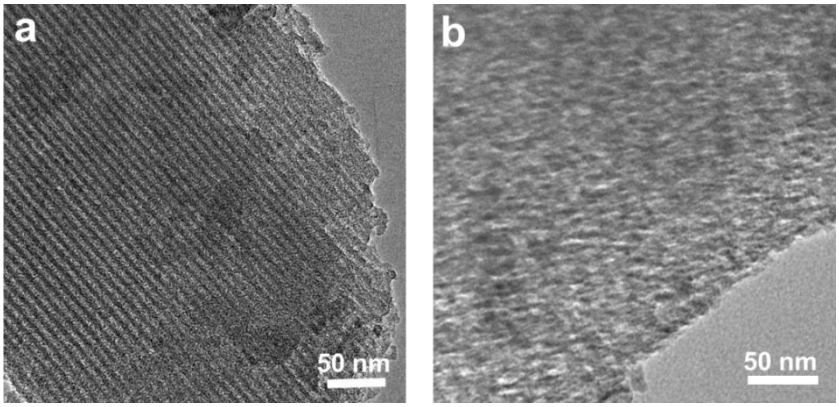

Figure S28. **Structural evolution of the mesoporous carbon, related to Figure 5.** TEM images of the mesoporous carbon before (a) and after (b) 1000 cycles at the current density of 0.4 $A \cdot g^{-1}$.

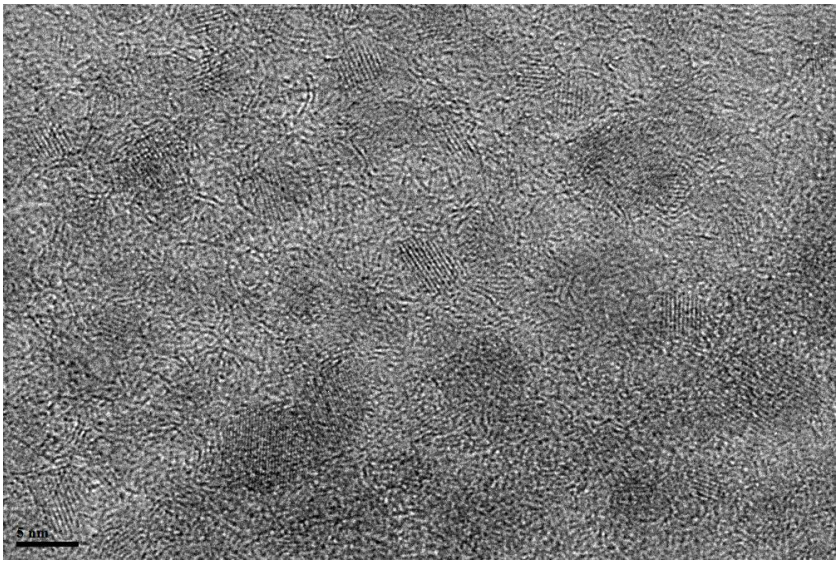

Figure S29. Structural evolution of the mesoporous TiO_2/TiC@C membranes, related to Figure 5.

HRTEM image of the mesoporous TiO_2/TiC@C membranes after 1,600 cycles at the current density of 0.4 $A \cdot g^{-1}$.

Table S1. Structural and textural properties of the mesoporous TiO_2@C and TiO_2/TiC@C membranes, related to Figure 2.

	S_{BET} (m^2/g)	S_{Micro} (m^2/g)	V (cm^3/g)	Dp (nm)
TiO_2/C	501	147	0.38	4.02
TiO_2/TiC@C	674	276	0.42	3.78

Table S2. A summary for the cycling performance of the ordered mesoporous TiO_2/C and TiO_2@TiC/C membranes, related Figure 3.

	Current density ($A\ g^{-1}$)	*Capacity**		*Capacity retention (%)*	*Coulombic efficiency (%)*	*Cycle number*
		Gravimetric capacity ($mAh \cdot g^{-1}$)	*Volumetric capacity ($mAh \cdot cm^2$)*			
TiO_2/TiC@C	0.4	244	705	85.1	99.3	1600^{th}
	1.5	150	434	68.4	99.4	5000^{th}
TiO_2/C	0.4	161	465	38.7	99.7	1600^{th}

*The results summarized from Figure 3c in the manuscript and Figure S16 in the supporting information. The capacities are calculated by active materials.

Table S3. Rate performance comparison between the TiO_2/TiC@C composite and mesoporous carbon，related Figure 3.

Current density (A g^{-1})	*Capacity (mAg^{-1})*		*Capacity ratio*
	TiO_2/TiC@C (TTC)	*mesoporous carbon (MC)*	*MC/TTC*
0.33	278	163	0.58
0.66	250	107	0.43
1	179	71	0.4
2	138	40	0.29
4	105	28	0.27
6	80	17	0.21
8	60	16	0.27
10	56	13	0.24
0.33	280	170	0.61

*The result summarized from Figure 3b in the manuscript and Figure S19 in the supporting information.

Transparent Methods

Materials Synthesis

Preparation of resol precursors: The phenolic resol precursors were prepared according to the previous report (Zhao et al., 2005). In a typical synthesis, 8.0 g of phenol was melted in a flask at 45 °C and then mixed with 1.68 g of NaOH solution (20 wt %) under stirring. After 10 min, 13.76 g of formalin (37 wt % formaldehyde) was added dropwise. Upon further stirring for 1 h at 70 °C , the mixture was cooled down to room temperature. The pH value was adjusted to ~7.0 by using 2.0 M HCl solution. Then the water was removed under vacuum at 49 °C . Finally, ethanol was added to precipitate NaCl and dissolve the resol to obtain a 20 wt % solution.

Preparation of titanium citrate complex: The preparation procedure for titanium citrate complex was similar to the previous report (Waterland et al., 2004). For a typical preparation, 28.4 g (100 mmol) of titanium isopropoxiede was dissolved in 50 mL of ethanol (solution A) and 21.0 g (100 mmol) of citric acid was dissolved in 100 mL of ethanol (solution B). Solution B was dropped into the solution A under stirring at 40 °C for 2 h. Ethanol was then removed by rotary evaporation at 40 °C then white powders were obtained. Water was added to dissolve the white powders to obtain 1.0 M homogeneous solution.

The mesoporous TiO_2@C and TiO_2/TiC@C composite membranes were synthesized *via* a universal strategy by using the phenolic resol (see Supplemental Experimental Procedures for details), pluronic F127 and the titanium citrate complex (see Supplemental Experimental Procedures for details) as a carbon precursor, template and titanium precursor, respectively. The silicon wafers were first treated with piranha solution (98% sulfuric acid:30% hydrogen peroxide = 2:1 v/v) at 90 °C for 30 min to form a thin silica oxide layer on the surface as substrates. In a typical synthesis, 1.5 g of F127, 2.5 g of the resol and 3.0 g of the titanium citrate solution were dissolved in 16 mL of water/ethanol mixture (1:1 v/v). After stirring for 30 min at room temperature, the solution was coated onto the pretreated silicon wafer (2 cm × 2 cm) at 600 rpm for 10 s to form a thin film. The film was dried at 40 °C for 3–5 h, followed by aging at 100 °C for another 24 h. The mesoporous TiO_2@C and TiO_2/TiC@C composite membranes on the silicon wafer were obtained after pyrolyzing at 700 and 900 °C for 2 h in nitrogen, respectively. The ramping rate was 1 °C min^{-1} below 600 °C, and 5 °C min^{-1} above 600 °C. To obtain free standing membranes, a polymethyl methactylate (PMMA) solution was spin-coated onto the composite membranes to increase the toughness. Afterward, the obtained membranes supported by PMMA thin films were immersed into a potassium hydroxide solution (10 wt %) at room temperature for 8–10 h to etch the silica layer on the surface of silicon wafer. After the PMMA film was dissolved by anisole, the free-standing membranes with a size of 2 cm × 2 cm were obtained.

Electrochemical Measurements

The electrochemical performances of the membrane electrodes were evaluated in 2016-type coin cells. The cells were set up by using the mesoporous TiO_2/TiC@C composite membranes standing on copper foils as work electrodes and commercial lithium disks as the counter electrodes, respectively. A non-aqueous solution of 1.0 M $LiPF_6$ in a 1:1:1

of ethylene carbonate (EC), diethyl carbonate (DEC), and dimethyl carbonate (DMC) was used as the electrolyte. For a flexible full cell, the commercial $LiCoO_2$ coating on aluminum foil was used as the counter electrode. The electrode was dried at 80 °C over night at a vacuum oven before assembly. All the cells were assembled in a glove box with $[O_2]$, $[H_2O] \leq 1$ ppm. Specific capacities were calculated based on the weight of membranes (~ 5 μm, ~0.5 mg). The galvanostatic charge/discharge test was conducted on LAND cycler (Wuhan LAND electronics Co., China) under ambient temperature. Cyclic voltammetry measurements were carried out at a scan rate of 1 $mV \cdot s^{-1}$ under the voltage range of 0.01 ~ 3 V by using a CHI 660e electrochemical workstation (Chen-Hua Instruments Co., China). Electrochemical impedance spectra were recorded using the Solatron 1260/1287 Electrochemical Interface (Solatron Metrology, UK) with oscillation amplitude of 5 mV at the frequency range from 100 mHz to 100 kHz.

Full Battery Assembly

To assemble a flexible full battery, a 30 × 30 mm^2 TiO_2/TiC@C anode was coupled with a $LiCoO_2$ cathode, which was prepared by coating conventional $LiCoO_2$ nanoparticle slurry on an Al foil (mass loading: ~ 3.0 mg cm^{-2}). Prior to the assembly, the TiO_2/TiC@C anode was prelithiated by placing it in direct contact with a wet Li foil and the electrolyte for 12 h to compensate its large initial irreversible capacity. The mass ratio of the TiO_2/TiC@C and $LiCoO_2$ in the full battery was adopted as 1:2, considering the difference in specific capacity of the two electrodes. The specific capacity is calculated based on the $LiCoO_2$ mass because the battery is cathode-limited. The battery was packaged with a flexible polyethylene foil bag by edge bonding machine, and the same electrolyte as used in the coin cells was injected when placed inside an argon-filled glovebox. The full batteries were cycled in the range of 2.8 – 4.2 V on LAND galvanostatic charge/discharge instruments.

Material Characterization

X-ray diffraction (XRD) patterns were collected by a Bruker D8 powder X-ray diffractometer (Germany) with Cu Kα radiation (40 kV, 40 mA). Small-angle X-ray scattering (SAXS) patterns were recorded by a Nanostar U small-angle scattering system (Bruker, Germany) with Cu Kα radiation (40 kV, 35 mA). GISAXS measurements were carried out at beamline BL16B1 of Shanghai Synchrotron Radiation Facility (SSRF). The incident X-ray photon energy was 10 keV and a MAR165 area detector was used to record the scattering intensity. The *d*-spacing values were calculated using the formula $d = 2\pi/q$, where $q=4\pi (\sin\theta)/\lambda$. Field emission scanning electron microscopy (FESEM) images were obtained on a Hitachi S4800 field-emission SEM (Japan) operated at 1 kV and 10 μA. Transmission electron microscope (TEM) measurements were conducted on a JEOL 2100F microscope (Japan) at 200 kV. For TEM measurements, the samples were prepared by sonication in ethanol and suspended on holey carbon grids. N_2 adsorption-desorption isotherms were measured with a Micromeritics Tristar 2420 analyzer at 77 K. Before measurements, the samples were degassed at 180 °C for more than 5 h. The Brunauer-Emmett-Teller (BET) method was utilized to calculate the specific surface areas. The pore size distributions were derived from the desorption branches of the isotherms based on Barrett-Joyner-Halenda (BJH) model. The total pore volumes were estimated from the

amount adsorbed at a relative pressure (P/P_0) of 0.995. Thermogravimetric analysis (TGA) curves were carried out using a Mettler Toledo TGA-SDTA851 analyzer (Switzerland) from 30 to 800 °C in an air flow of 80 mL min^{-1} at a heating rate of 10 °C min^{-1}.

Supplemental References:

Meng, Y., Gu, D., Zhang, F., Shi, Y., Yang, H., Li, Z., and Zhao, D. (2005). Ordered mesoporous polymers and homologous carbon frameworks: amphiphilic surfactant templating and direct transformation. Angew. Chem. Int. Ed. 44, 7053-7059.

Kemmitt, T., Al-Salim, N.I., Gainsford, G.J., Bubendorfer, A. and Waterland, M. (2004). Unprecedented oxo-titanium citrate complex precipitated from aqueous citrate solutions, exhibiting a novel bilayered Ti_8O_{10} structural core. Inorg. Chem. 43, 6300-6306.